INVESTIGATING THE IMPACTS OF ENTRAINMENT ON NUCLEATION SCAVENGING OF BLACK CARBON PARTICLES THROUGH PARTICLE-RESOLVED SIMULATIONS

BY

AMANDA JONES

THESIS

Submitted in partial fulfillment of the requirements
for the degree of Master of Science in Atmospheric Sciences
in the Graduate College of the
University of Illinois at Urbana-Champaign, 2014

Urbana, Illinois

Adviser:

Assistant Professor Nicole Riemer

Abstract

Aerosol particles have the ability to alter our climate by direct and indirect effects. Black carbon is a unique aerosol in that along with scattering, it can also absorb solar radiation, which heats the atmosphere and contributes to a positive radiative forcing. The optical and cloud condensation nuclei properties of the aerosol depend on the per-particle chemical species composition, or mixing state. Challenges arise in determining black carbon climate effects because the mixing state changes during the particles' transport in the atmosphere. By condensation of semi-volatile substances, coagulation, and photochemical processes, termed aging, the mixing state of the particles change can further change. During the aging processes, initially hydrophobic black carbon become hydophilic, and can then act as cloud condensation nuclei. Under a high supersaturation, the particles can form cloud droplets, altering the cloud albedo and radiative forcing. To characterize the radiative effects of black carbon, knowledge of condensational growth and activation are important. In determining the particle evolution, it is necessary to consider entrainment of dry air into a cloud in order to achieve the cloud droplet spectra.

In our current research, we used the particle-resolved model PartMC-MOSAIC, which has the ability to track the individual size and composition of thousands of particles through the aging processes of condensation, coagulation, and chemistry. Through PartMC-MOSAIC, an urban plume scenario was simulated and an aged particle population was determined every hour. Then, the particle populations were used as input into a particle-resolved cloud parcel model. Previously, the cloud parcel was assumed to be adiabatic. In this work, we tested the cloud parcel model capability with entrainment implemented through a homogeneous

approach.

We presented three cases in this work. Case 1 used idealized temperature, pressure, and total specific humidity profiles to extend the study by *Ching et al.* (2012) to include entrainment. Case 2 used idealized total specific humidity profiles and less idealized temperature and pressure profiles, constructed from 3-D cloud resolving data. Finally, Case 3 used composition-averaged particle populations initialize the cloud parcel and we used Case 2 as a reference case to compare the results.

For Case 1, entrainment caused a decrease in the cloud droplet number concentration (CDNC) and the liquid water content (LWC) according to the amount of entrainment. In Case 2, the CDNC and LWC followed the same pattern as Case 1 when using T_2 profiles, while the CDNC was higher than the no entrainment case for the scenarios with T_1 profiles. The size distribution broadened and shifted towards smaller sizes. In Case 3, a large overestimation in the black carbon nucleation scavenged mass fraction, f_{BC} and a small difference in the cloud droplet fraction, f_{N} was seen for all plume hours in the compostition averaged case compared to the reference case. Entrainment altered f_{BC} and f_{N} for scenarios using T_1 profiles.

To my loving parents and supportive friends

Acknowledgments

I would like to thank my advisor, Dr. Nicole Riemer for her guidance, support, and dedication during my time here at the University of Illinois. I have learned so much from this experience, and appreciate the effort and support you give your students. I would also like to thank the members of the Riemer research group including Wayne Chang, Jeffrey Curtis, Laura Fierce, Zaneta Gacek, Swarnali Sanyal, Jian Tian, and Joseph Ching. They have guided my research journey and provided countless suggestions and help along the way. I would also like to thank all the faculty and staff at DAS for being so invested in the students and sharing their love of atmospheric science with me.

Finally, I would not be where I am today without the love and encouragement from my parents. I also want to thank all my friends who have gone through this process with me. I could not have done it alone.

Table of Contents

Chapter 1

Introduction

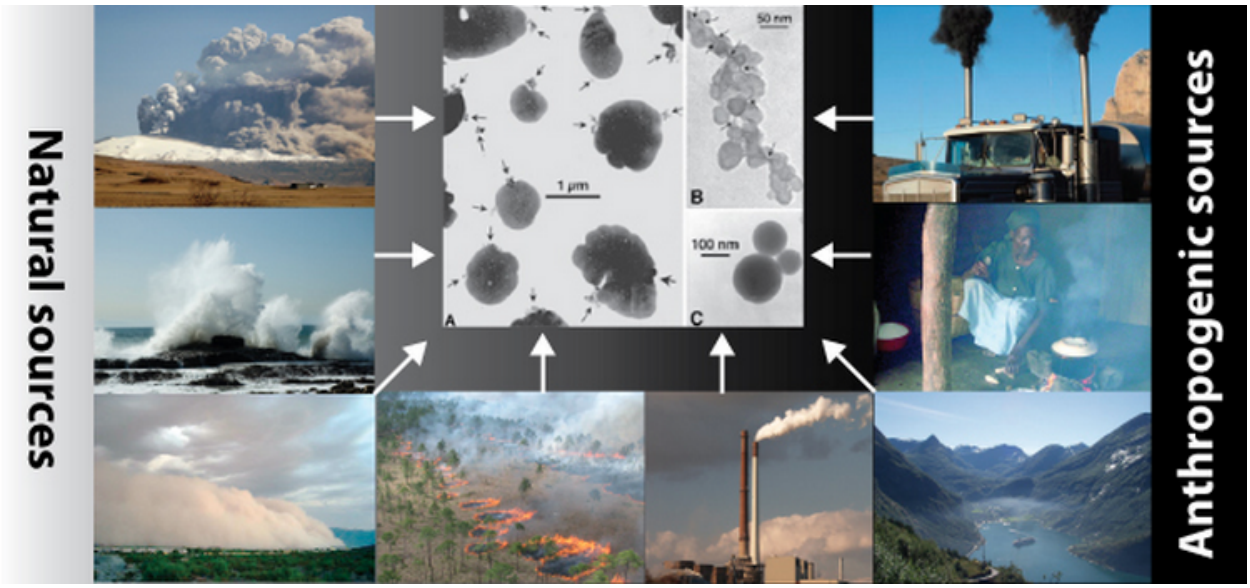

Figure 1.1: Natural and anthropogenic sources of aerosols (*Myhre et al.*, 2013).

Aerosol particles are solid or liquid particles suspended in the atmosphere. Primary aerosols are directly emitted as particles while secondary aerosols can either be formed by condensing vapors from precursor gases or by nucleation (*Myhre et al.*, 2013). Aerosols vary in their chemical composition depending on their source and formation process, and they can originate from both natural and anthropogenic sources. Some natural sources include volcanoes, oceans, and deserts, while anthropogenic sources include road transport, cooking, ships, and coal power plants, which is illustrated in Figure 1.1.

Aerosol particles impact our health, visibility and climate. Aerosols can have direct effects on the climate by absorption and scattering of solar radiation. The chemical composition of individual particles, or the aerosol mixing state is altered through the aging processes of co-

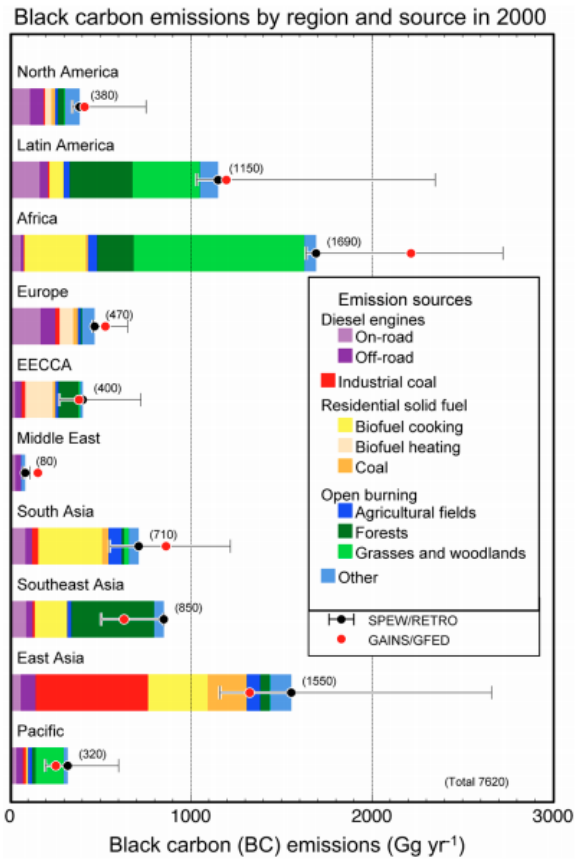

Figure 1.2: Emission rates of black carbon in the year 2000 by region. The color bars represent major source categories in each region (*Bond et al.*, 2013).

agulation, condensation and photochemistry (*Riemer et al.*, 2009). These aging processes of the aerosols affect the particles' size and chemical composition, which will in turn alter their effect on climate (*Myhre et al.*, 2013). For example, aging can increase the hygroscopicity of the aerosols, which increases their ability to become cloud condensation nuclei. Therefore, aerosol particles can also contribute to an indirect radiative effect through by altering cloud albedo (*Penner et al.*, 1993).

In this thesis, we focus on the aerosol-cloud interactions of black carbon-containing particles. Major sources of black carbon include diesel engines, industry, residential solid fuels, and open burning (*Bond et al.*, 2013). In the year 2000, diesel engines contributed to roughly half of the black carbon emissions in North America, as seen in Figure 1.2, where gasoline engines contributed to a smaller percentage of the emission rates as represented in the 'Other'

category. In this study, we focus on gasoline and diesel vehicle emissions in an urban setting.

Black carbon particles contribute both to the direct and indirect climate effects, and the aging processes plays an important role. Black carbon is a strong absorber of solar radiation the aging of black carbon increases light absorption. Further, during the aging process, initially hydrophobic black carbon particles can become hydophilic and can then act as cloud condensation nuclei more easily. This alters the cloud microphysics, and affects the cloud lifetime as well as the lifetime of black carbon.

Previous work by *Ching et al.* (2012) developed a framework to investigate the importance of black carbon mixing state by using the particle-resolved model PartMC-MOSAIC coupled with a cloud parcel model. Results showed that the per-particle composition is important for determining the mass concentration of black carbon that is incorporated in a cloud, and not as important for determining the total number concentration of cloud droplets. One limitation of the work was that the cloud parcel was assumed to be adiabatic, i.e. entrainment effects were not included in the simulations. While this may be a good assumption for the undiluted core of a cloud, we know that entrainment can be of great importance for cloud edges. The turbulence in convective clouds leads to entrainment of subsaturated air, which affects the microphysical properties within the cloud. It has been observed that entrainment depletes the liquid water content (LWC), broadens the size distribtution, and increases collision-coalescence, therefore, increasing the production of rain drop embryo (*Cooper et al.*, 2013; *Blyth et al.*, 2005).

In this study, we revisit the investigation of *Ching et al.* (2012), but now include entrainment of non-cloudy air into the cloud. We use data from a three-dimensional cloud resolving model to construct scenarios that investigate the impact of the amount of entrainment, cooling rate, and mixing state on cloud liquid water content, cloud droplet number concentration, and number concentration size distribution and the nucleation-scavenging of black carbon. The contribution of this study is to 1). test the new model capability, which includes the implementation of the entrainment process 2). investigate the impact of entrainment and

black carbon mixing state on cloud microphysical properties and nucleation-scavenging of black carbon particles.

Chapter 2

Background

Black carbon has a significant impact on our climate and health. Along with climate impacts, black carbon-containing particles are small enough to enter the respiratory tract and are associated with adverse health impacts including asthma and decreased lung function (*Gardiner et al.*, 1993). In this thesis, we focus on the black carbon climate effects. This chapter will begin with the definition of black carbon and a review of black carbon climate impacts including the so-called direct and indirect effects. Next, the definition of aerosol mixing state and the process of aerosol aging will be discussed along with the representation of aerosols in models. In order to discuss aerosol-cloud interactions, we end this chapter by reviewing the process of entrainment in clouds including the types of mixing and the effects on microphysics.

2.1 Black Carbon-Containing Particles

Currently, there are issues in defining black carbon in the scientific literature and there is no clear terminology when quantfying carbonaceous matter in aerosols. Difficulties in terminology arise because black carbon does not exist in the atmosphere as a pure substance and measurements of this particle type depend on the method used. Carbonaceous aerosols contain semi-volatile organic carbon (OC) and nonvolatile elemental carbon (EC). *Jeong et al.* (2004), showed that measured carbon fractions depend on the measurement method and need to be well defined operationally. The study suggested that the term black carbon be reserved for optical measurements and the term elemental carbon for thermal measurements.

Most black carbon loading in the atmosphere comes from anthropogenic sources including diesel engines, industry, residential solid fuels, and open burning (*Bond*, 2007). The type of fuel used to burn yields different amounts of black carbon per amount of fuel burned. For example, diesel engines produce more grams of black carbon per amount of fuel burned then gasoline (*Ogren and Charlson*, 1983). The burning process also impacts the density and refractive index of the particles (*Chỳlek et al.*, 1995).

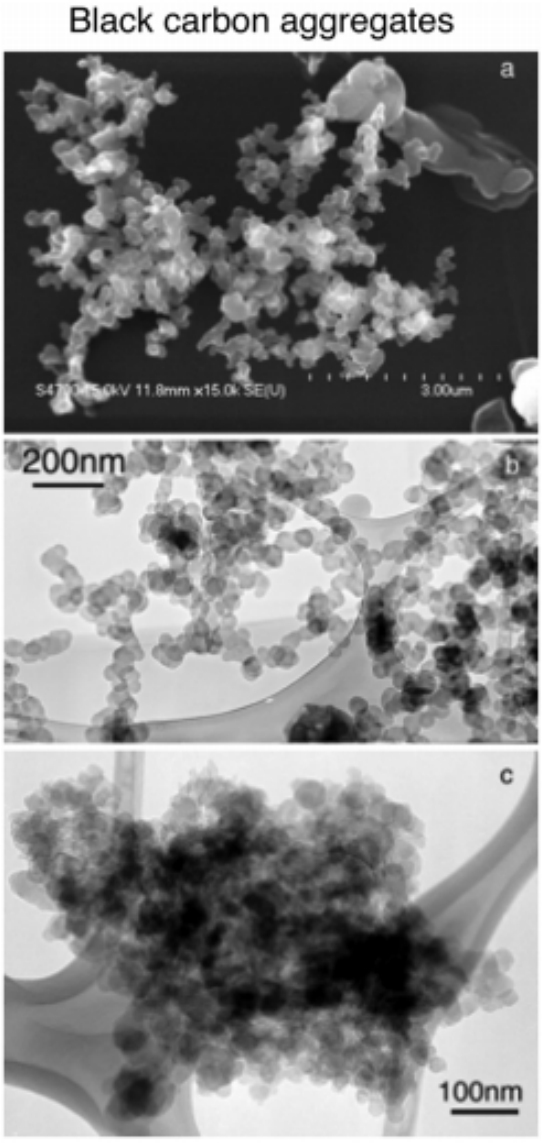

Figure 2.1: Various images of BC aggregates (*Bond et al.*, 2013).

The microstructure of black carbon is a graphite-like structure containting many sp^2-

bonded carbon atoms, which explain the ability of black carbon to absorb visible light (*Petzold et al.*, 2013). Black carbon exists as an agglomerate of roughly spherical carbon particles ranging from < 10 to 50 nm, which attach to form straight or branched chains (*Seinfeld and Pandis*, 2012; *Goldberg*, 1985; *Petzold et al.*, 2013). Figure 2.1 shows scanning electron microscope and transmission electron microscope images of black carbon aggregates. Black carbon-containing particles are refractory material, which volatizes near 4000 K. This leads to high stability in the atmosphere and a long atmospheric lifetime. These particles are insoluble in water are slowly removed by clouds, unless coated with water-soluble compounds (*Petzold et al.*, 2013). In this thesis, we define black carbon-containing particles as light-absorbing carbonaceous substances in an atmospheric aerosol. Hereafter, black carbon-containing particles will be referred to as BC particles.

2.2 Black Carbon Climate Impacts

BC particles have important impacts on climate because of their interactions with radiation. These are typically divided into direct and indirect effects. A way to quantify the impact of aerosols on the radiative budget of the Earth is to calclulate a radiative forcing of climate change. Radiative forcing is defined by the IPCC as the net change in the energy balance of the Earth system due to some imposed perturbation. For example, comparing present day conditions to preindutrial conditions, the global mean radiative forcing of CO_2 has a large positive forcing of $+2.83$ Wm^{-2} with an uncertainty of [$+0.17$ to $+1.48$ Wm^{-2}]. The largest uncertainties in determining the total anthropogenic radiative forcing are associated with the impact of aerosols (*IPCC*, 2013).

2.2.1 Direct Effects of Black Carbon

While most aerosols have a negative radiative forcing, BC is unique in that along with scattering, it can also absorb solar radiation, which heats the atmosphere and contributes

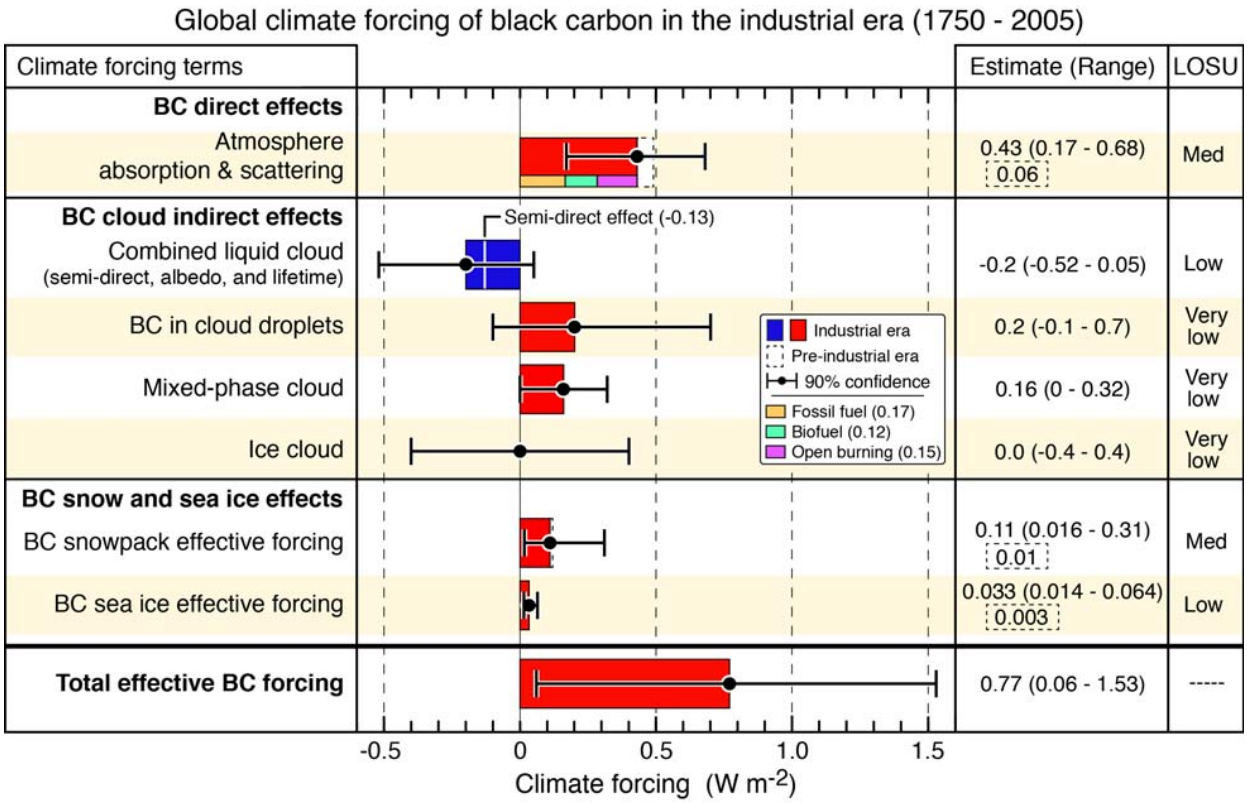

Figure 2.2: Globally averaged climate forcing. Bars represent uncertainties due to BC on the climate forcings (*Bond et al.*, 2013).

to a positive radiative forcing, seen in Figure 2.2. However, our understanding of black carbon climate forcing still contains large uncertainties. Since BC concentrations vary locally, radiative forcing estimates vary locally as well, so it is useful to calculate the global mean direct radiative forcing. The current radiative forcing estimate compares model estimates with present-day emissions and model estimates with emissions from 1750. The globally averaged climate forcing of black carbon is +0.71 Wm^{-2} with 90% uncertainty bounds of [+0.08 to +1.27 Wm^{-2}], which corresponds to a warming effect. This estimate comes from an average of radiative forcing estimates from global aerosol models with a scaling factor to correct for an underestimation of absorption by black carbon in many models. Reduction in BC emissions could offset increasing temperatures (*IPCC*, 2013). Uncertainties arise because the optical properties are difficult to determine. For example, the strength of absorption depends on the black carbon refractive index, the size and shape of the particle, the medium

in which the particle is embedded, the size of the host droplet, and the exact location of the black carbon within the host (*Chỳlek et al.*, 1995; *Videen et al.*, 1994).

2.2.2 Indirect Effects of Black Carbon

Indirect effects occur when aerosols, including BC, alter cloud properties, which in turn changes the radiative forcing. Aerosols alter the amount of radiation that is absorbed or scattered through the first indirect effect, also know as the Twomey effect (*Twomey*, 1977). Aerosols acting as cloud condensation nuclei (CCN) can increase the cloud droplet number concentration, so that for the same liquid water content, the cloud will consist of more but smaller droplets. This increases the brightness of the cloud and the amount of reflected radiation, which leads to a negative radiative forcing. This change in droplet number concentration contributes to the second indirect effect, where the lifetime of the cloud is altered because the smaller droplets collide less efficiently. This inhibits precipitation, increases the liquid water in the cloud, and creates more reflective clouds increasing the indirect forcing (*Albrecht*, 1989).

Additionally, there are various semi-direct effects of BC on the climate depending on the location of BC relative to the cloud layer. The semi-direct was first described by *Hansen et al.* (1997) as absorbing aerosols in or near a cloud layer can heat the layer and promote cloud evaporation. This has been shown to decrease low and high-altitude clouds (*Ackerman et al.*, 2000). Alternatively, BC located below the cloud layer destablilizes the atmosphere, increases convective activity, which increases cloud cover (*McFarquhar and Wang*, 2006; *Koch and Genio*, 2010). Furthermore, BC above cumulus clouds may suppress cumulus cloud development as observed in the Amazon Basin (*Koren et al.*, 2004) and simulated by *Fan et al.* (2008). Black carbon cloud indirect effects contribute to both positive and negative forcing. The combined liquid cloud effects have a radiative forcing of -0.2 Wm^{-2} with a [-0.61 to $+0.1$ Wm^{-2}] uncertainty range as seen in Figure 2.2. Due to lack of modeling studies on BC indirect effects, the cloud effects contain the largest uncertainty in

determining the impact of BC on Earth's radiative budget (*Bond et al.*, 2013). In addition, BC deposited on snow can reduce the albedo due to differences in the mass absorption cross section between ice and BC, further complicating the climate impacts of BC (*Bond et al.*, 2013).

2.2.3 Aerosol Aging and Black Carbon Mixing State

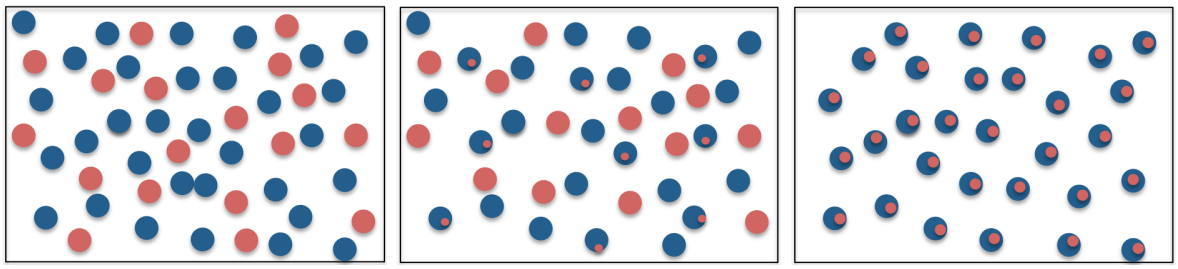

Figure 2.3: An illustration of a completely externally mixed population (left), an intermediate population (center), and a completely internally mixed population (right).

Challenges arise in determining BC climate effects because the composition on a per-particle level changes during the particles' transport in the atmosphere. Through condensation of semi-volatile substances, coagulation, and photochemical processes, termed aging, the mixing state of the particles change can further change (*Weingartner et al.*, 1997). The mixing state influences the refractive index, size, and density of the BC particles, which affects the optical properties. The aging of BC increases light absorption. A study by *Lesins et al.* (2002) found large differences in optical properties between an external and internal mixture of black carbon and ammonium sulfate. Knowledge of the optical properties affected radiative forcing calculations. In general, the external mixture predicted more cooling than the homogenous internal mixture. During the aging process, initially hydrophobic BC can become hydophilic, which can then act as cloud condensation nuclei. Under a high supersaturation, the particles form cloud droplets, a process known as black carbon-nucleation scavenging. This can reduce the BC atmospheric lifetime due to removal by precipitation (*Stier et al.*, 2006). Hence, the aging process alters BC climate effects including the direct

effect and indirect effects.

In this context, the term mixing state is often used. We define the mixing state of the aerosol population as the distribution of the per-particle chemical species compositions from (*Riemer and West*, 2013). Figure 2.3 depicts three different type of mixing states of an aerosol population containing two chemical species. The population is considered externally mixed if the different aerosol species are present in different particles. An internally mixed population consists of particles that contain different species. The population is fully internally mixed if all the particles have the same fraction of chemical species within the particle. The mixing state can exist somewhere between these two extremes, with one example seen in the center panel of Figure 2.3. Fresh emissions can be internally mixed when they enter the atmosphere if more than one component is involved in creating the aerosol. This is expected for BC particles since they originate from the combustion of complex mixtures like fossil fuels (*Lesins et al.*, 2002). Therefore, understanding aerosol aging is closey related to understanding the aerosol mixing state evolution. In order to adequately model climate impacts of aerosols, models need to represent the aging processes and mixing state.

2.3 Model Representation of Black Carbon

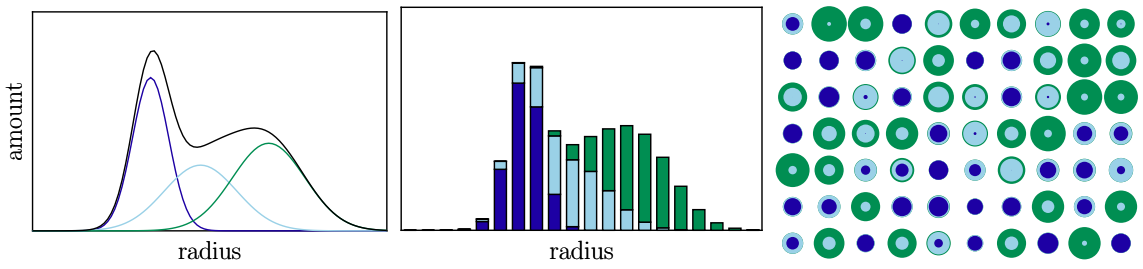

Figure 2.4: Schematic showing different aerosol model representations. Modal model (left), sectional model (center), particle-resolved model (right)

Most of the current models that represent BC use a distribution-based approach with a modal or sectional representation. In a modal approach, the aerosol are grouped into

independent sub-populations, or modes. Each mode has a size distribution function, which represents the size distribution of the aerosols. Advantages of modal models include being computationally fast and containing a flexible model structure. The limitations are that the accuracy depends on the mode distibution functions (*Whitby and McMurry*, 1997). Another common approach is the sectional representation. This method divides the aerosol size distribution into sections depending on the size, volume or other aerosol quantities. The chosen quanitity is conserved within the domain. Sectional models are flexible in their structure, but can be computationally expensive since the accuracy depends on the number of sections used (*Gelbard and Seinfeld*, 1980). Both modal and sectional approaches group aerosols, which loses the characteristics of individual particles within one bin or mode (*Spracklen et al.*, 2005). In many global models, the aging process is represented by an aging timescale on which BC particles transfer from a fresh sub-population to an aged sub-population. This is a constant value of around one day. Models are sensitive to this value and it is not very well constrained (*Riemer et al.*, 2009).

A different modeling approach, more suited to represent mixing state, is particle-resolved modeling. *Riemer et al.* (2009) simulated the evolution of soot mixing state with a stochastic particle-resolved model, PartMC-MOSAIC. The model has the ability to track the size and composition of hundreds of thousands of particles, evolving in a particular scenario, undergoing aging processes. With the capabilities of this particle-resolved model, the evolution of the mixing state is tracked and the particle composition is not lost in the model representation. *Ching et al.* (2012) coupled PartMC-MOSAIC with a cloud parcel model to investigate the impact of black carbon mixing state on black carbon nucleation scavenging. Results showed that the per-particle composition is important in knowing the mass of black carbon in the cloud, and not as important for the total number of cloud droplets. However, entrainment was not included in the cloud parcel model. This neglects an important process within cumulus clouds and more work is needed to fully quantitatively investigate BC nucleation scavenging. The study by *Ching et al.* (2012) serves as the motivation for

our work, and we will build on it, by including the entrainment process. More details on PartMC-MOSAIC and the cloud parcel model capability is given in Chapter 3. For the remainder of this chapter, the entrainment process will be reviewed.

2.4 The Process of Entrainment of Non-cloudy Air

It has been shown that subsaturated air enters a cloud, a process called entrainment, which affects the microphysical properties within the cloud. *Stommel* (1947), was the first to develop the idea of entrainment in cumulus clouds. This theory involves non-cloudy air entraining into the cloud similar to a jet stream. For example, when a jet moves through a fluid, there is entrainment of the surrounding fluid into the jet. It was not until 1953 that the thermal model was presented. *Scorer and Ludlam* (1953) described convection as a rising bubble of warm air where surrounding air mixes into the wake of the bubble. Later work by *Scorer* (1957) describes the entrainment process involving a shedding thermal model. In this model, small thermals ascend and continually mix in environmental air through the cloud tops. The entrained air is then deposited in the trailing wake. More recent experiments have shown that air can enter through the rear by penetrative downdrafts (*Johari*, 1992; *Squires*, 1958). These strong downdrafts driven by overshooting cloud tops contribute to mixing and detrainment of cloudy air as parcels decsend to a neutrally buoyant state (*Telford*, 1975). A study by *Carpenter Jr et al.* (1998), found undilute boundary layer air in the thermals at all vertical layers of the cloud. Through the use of a three-dimensionsal cloud model, the shedding thermal model was confirmed. The rising thermals eroded and entrained air was deposited into the wake. Penetrative downdrafts also contributed to the mixing of the dry air as well as detrainment of mass and moisture. The circulation around thermals in Florida cumulus clouds studied in *Blyth et al.* (2005), were observed to be similar to the flow observed in laboratory thermals in *Scorer* (1957). This flow occured via updrafts in the center of the cloud and downdrafts at the edges of the updraft or cloud.

2.4.1 Entrainment Mixing Processes

Mixing of sub-saturated air into the cloud affects the droplet population. Assuming the classical homogenous process, droplets anywhere in the cloud are exposed to the same relative humidity. In 1977, the mixing process of non-cloudy and cloudy air was alternatively described as inhomogenous. The droplets close to the entraining dry air were greatly affected, and the droplets far from the entrainment were less affected, or not affected at all (*Latham and Reed*, 1977). To determine the type of mixing, *Baker et al.* (1980) compared the timescales of rate processes of turbulent diffusion of the entrained air and evaporation of a droplet under subsaturated conditions. The type of mixing depended on the magnitude of the timescales. If the turbulent mixing timescale is much larger than the droplet evaporation timescale, all droplets will evaporate equally, following the classical homogenous process. The opposite case leads to an inhomogenous limit, in which the slow mixing evaporates some droplets, but not others. In the inhomogenous model, the largest droplets grew by condensation around three times faster than the homogenous model due to higher supersaturations. In this work, we assume homogenous mixing of the sub-saturated air with the cloud parcel. The justification will be presented in the Chapter 3.

2.4.2 Entrainment Effects on Microphysics

Entrainment of sub-saturated air is an important process because it changes the microphysical quantities of the cloud. It has been observed that entrainment depletes the liquid water content (LWC) (*Blyth et al.*, 2005). A study by *Barahona and Nenes* (2007), developed a critical entrainment rate to calculate the limit where entrainment prevents supersaturation and cloud droplet formation. If the entrainment rate is below the critical rate, supersaturation occurs and CCN can activate to form cloud droplets. Above the critical level, mixing prevents activation. Entrainment affects other microphysical properties including droplet size distributions.

Telford and Chai (1980) speculated that entrainment at cloud top can explain the production of large droplets. Their work showed that the mixing process increases maximum drop sizes. The entrainment occured in cycles, diluting the cloud from the top down. This downward moving air mixed with upward moving air, decreasing the number of droplets. The fewer number of droplets under the supersaturation grew to larger sizes than without the mixing. *Baker et al.* (1980) also saw broadening of droplet distibutions towards larger sizes under an inhomogenous mixing approach. Under this assumption, more droplets are completely evaporated and newly formed cloud droplets cannot compete as effectively for the available water vapor. The supersaturation will be larger than the homogenous case and drops not affected by the entrainment will grow faster. In their work, the broadened spectra under the inhomogenous mixing approach agreed with observations. Furthermore, *Lasher-Trapp et al.* (2005) used a three-dimensional cloud model coupled with a Lagrangian microphysical parcel model to investigate changes in the droplet size distribution due to entrainment in warm cumulus clouds. Results show broadened distributions due to the variablility of entrainment. Droplets encountered different supersaturations during the time in the cloud. In *Cooper et al.* (2013), the effect of entrainment on droplet size distributions was used to study the production of rain in cumulus clouds. The study used a high-resolution microphysical model along with trajectories from a three-dimensional cloud model to study the mixing process. Entrainment was shown to enhance diffusional growth and production of raindrops dependent upon the variability along the trajectories. The results showed a broadened distribution, which increased collision-coalescence and therefore the production of rain drop embryos. There are still questions that need to be answered to fully understand the entrainment process and how it affects the liquid water content, drop size distribution, and other microphysical quantities. This will ultimately increase the understanding of cloud optical properties and precipitation efficiency (*Burnet and Brenguier*, 2007).

2.5 Outline of Research

Chapter 3 describes PartMC-MOSAIC, the particle-resolved aerosol model. Within a Lagrangian parcel framework, we simulated the evolution of aerosol particles in a parcel of air through an idealized urban setting. The governing equations of the model and the description of the cloud parcel model, including the addition of entrainment are presented in this chapter. Chapter 4 describes the urban plume simulation setup and results. This urban plume scenario was used to initialize the cloud parcel model. Chapter 5 describes the cloud parcel simulation setup and results. Last, a summary of our work is presented in Chapter 6.

Chapter 3

Model Description

This work used the particle-resolved model PartMC-MOSAIC in conjunction with a particle-resolved cloud parcel model. In this chapter, we give a brief description PartMC-MOSAIC and the cloud parcel model, including the addition and entrainment.

3.1 PartMC-MOSAIC

A detailed model description of the particle-resolved model PartMC-MOSAIC is provided in *Riemer et al.* (2009). PartMC-MOSAIC which has the ability to track the composition of thousands of particles. Since the composition of every particle is resolved, there are no a priori assumptions about mixing state, and the numerical solution is not subject to numerical diffusion.

PartMC-MOSAIC simulates the evolution of particles and gases with a Langrangian parcel of air moving along a prescribed trajectory. This is a box model where the mass of each species within one particle is tracked, but not the particle position. The model also includes emissions of aerosols and gases and dilution with background air. The modeled volume is representative of a larger volume of air. The Langrangian parcel has a computational volume, V_{comp} where the aerosol population in the volume is represented by storing N_{p} particles, written Π=($\vec{\nu_1}$, $\vec{\nu_2}$..., $\vec{\nu}_{n_{\text{p}}}$), where the particle order is not significant. Each particle is an A-dimensional vector $\vec{\nu_i} \epsilon \mathbb{R}^A$ with components (ν_i^1, ν_i^2, ..., ν_i^A), where ν_i^a is the volume of species a in particle i for $a = 1$, ..., A and $i = 1$,..., N_{p}. The aerosol number concentration

distribution at time t, $n(\vec{\nu}, t)$ is defined as

$$n(\vec{\nu}, t) = \frac{\partial^A N(\vec{\nu}, t)}{\partial \nu_1 \partial \nu_2 ... \partial \nu_A}. \tag{3.1}$$

Throughout the simulation, the aerosol population can change via two mechanisms. First, the particles in the simulation change by addition and removal of emissions, dilution or coagulation between particles. In *Riemer et al.* (2009), a multiscale stochastic coagulation method was developed to make the particle resolved method computationally affordable. It uses binned sampling to sample from the mulitscale Brownian coagulation kernel for non-uniform particle distributions. Second, each particle can change composition through species that condense from the gas phase, which changes the vector v_i for particle i. The model tracks the mixing state as the particles evolve. In this work, PartMC is coupled with the deterministic gas and aerosol chemistry code MOSAIC. It contains a state-of-the-art dynamic gas-particle partitioning module coupled to a thermodynamics module, along with an algorithm for mass transfer to mixed-phase and solid particles, and gas-particle partitioning. These processes are performed deterministically (*Zaveri et al.*, 2008).

MOSAIC treats the major aerosol species important in the urban through global scales including sulfate, methanesulfate, nitrate, chloride, carbonate, ammonium, sodium, calcium, black carbon, primary organic mass, and liquid water. Unspecified inorganic species, inert material, and trace metal are included in other inorganic mass. The gas-phase species including sulfuric acid, nitric acid, hydrochloric acid, ammonia, and methanesulfonic acid are allowed to partition to the particle phase (*Zaveri et al.*, 2008). MOSAIC includes four computationally efficient modules including the photochemical mechanism CBM-Z based off the carbon-bond mechanism, (*Zaveri and Peters*, 1999) the multicomponent Taylor expansion method (MTEM) for estimating activity coefficients of electrolytes and ions in aqueous solutions (*Zaveri et al.*, 2005b), the multicomponent equilibrium solver for aerosols (MESA) for intra-particle solid-liquid partitioning (*Zaveri et al.*, 2005a), and the adaptive step time-split

Euler method (ASTEM) for dynamic gas-particle partitioning over size and composition resolved aerosol (*Zaveri et al.*, 2008). Secondary organic aerosol (SOA) is included in this version of MOSAIC through the SORGAM scheme, which simulates SOA formation including the production of low-volatility products and gas/particle partitioning (*Schell et al.*, 2001).

3.2 Cloud Parcel

Ching et al. (2012) coupled PartMC to a particle resolved cloud parcel model, which simulates particles competing for water vapor while the parcel is exposed to a prescribed cooling. Surface tension effect on droplet growth, sedimentation, coagulation, chemical transformation, and entrainment in the cloud parcel were not included. The study investigated the impacts of mixing state on on black carbon nucleation scavenging. In our work, entrainment is added to the cloud parcel model to investigate if the conclusions in *Ching et al.* (2012) still hold.

During the cloud parcel simulation, a system of ordinary differential equations is solved involving a coupled pair of equations describing a multidimensional aerosol distribution and the concentration of the gas phase, respectively.

$$\frac{n(\vec{\nu},t)}{\partial t} = \lambda_{\text{entrain}}(t)(n_{\text{back}}(\vec{\nu},t) - n(\vec{\nu},t)) - \frac{\partial}{\partial \nu_{\text{C+1}}}(c_{\text{w}} I_{\text{w}}(\vec{\nu},\vec{g},t))n(\vec{\nu},t) \tag{3.2}$$

$$\frac{dg_i(t)}{dt} = \lambda_{\text{entrain}}(t)(g_{\text{back},i}(t) - g_i(t)) - \int_0^\infty \int_0^\infty ... \int_0^\infty I_{\text{w}}(\vec{\nu},\vec{g},t)) \times n(\vec{\nu},t) d\nu_1 d\nu_2 ... d\nu_A + \frac{1}{\rho_{\text{dry}}(t)} \frac{d\rho_{\text{dry}}(t)}{dt} g_i(t), \tag{3.3}$$

where $n(\vec{\nu},t)$ (m^{-3} $\text{kg}^{-\text{A}}$) is the aerosol number distribution at time t as defined in 3.1, $n(\vec{\nu},t,\text{back})$ (m^{-3} $\text{kg}^{-\text{A}}$) is the background aerosol number distribution. The entrainment rate is λ_{entrain} and will be defined in section 3.3.1. The background concentration of gas species i is $g_{\text{back}}(t)$ (mol m^{-3}), I_{w} $(\vec{\nu})$ $(\vec{\nu},g,t)$ (mol^{-1} s^{-1}) is the condensation flux for water

and c_{w} (kg mol^{-1}) is a conversion factor for water.

A condensational growth equation for each particle is solved, together with the equation for the rate of change of environmental saturation S_{v}. S_{v} and D_i, the wet diameter of particle i, describe the state of the system. The condensational growth rate $\dot{D}_i$ of aerosol particle i is

$$\dot{D}_i = \frac{4D'_{\mathrm{v},i}M_{\mathrm{w}}P^0}{\rho_{\mathrm{w}}RTD_i}(S_{\mathrm{v}} - a_{\mathrm{w},i}\frac{1}{1+\delta_i} \times \exp(\frac{4M_{\mathrm{w}}\sigma_{\mathrm{w}}}{\rho_{\mathrm{w}}RTD_i}\frac{1}{1+\delta_i} + \frac{\Delta H_{\mathrm{v}}M_{\mathrm{w}}}{RT}\frac{\delta_i}{1+\delta_i})) \tag{3.4}$$

$$\delta_i = \frac{\Delta H_{\mathrm{v}}\rho_{\mathrm{w}}}{4k'_{\mathrm{a},i}T}D_i\dot{D}_i, \tag{3.5}$$

where $D'_{\mathrm{v},i}$ is the corrected diffusivity coefficient for particle i, $a_{\mathrm{w},i}$ is the water activity of particle i, σ_{w} is the water surface tension, ΔH_{v} is the specific latent heat of vaporization of water, $k'_{\mathrm{a},i}$ is the corrected thermal conductivity of air for particle i, T is the environmental temperature, ρ_{w} is the density of water, M_{w} is the molecular weight of water, R is the universal gas constant, and P^0 is the saturation vapor pressure.

The Köhler equation is adapted to the κ hygroscopicity parameterization to relate particle dry diameter to CCN activity (*Petters and Kreidenweis*, 2007). The volume of ν_{i}^a of each particle i is fixed for each species a except water, where water is the Ath species. The volume of water in particle i is $\nu_{\mathrm{i}}^{\mathrm{w}} = \nu_{\mathrm{i}}^A$. This varies with the wet diameter D_i by

$$\nu_i^{\mathrm{w}} = \nu_i - \nu_i^{\mathrm{dry}}, \tag{3.6}$$

where $\nu_i = \frac{\pi}{6}(D_i)^3$ represents the total volume and ν_i^{dry} is the dry volume. This quantity is calculated by summing the volumes of the non-water species by

$$\nu_i^{\mathrm{dry}} = \sum_{i=1}^{A-1}\nu_i^a. \tag{3.7}$$

The volumes will be used in calculating the mixing rule assumptions of the hygroscopicity parameters in (*Petters and Kreidenweis*, 2007). The hygroscopicity parameter κ relates the dry particle volume (V_{dry}) and liquid water volume (V_{w}) in particle i to its water activity by

$$a_{\mathrm{w},i} = \frac{\nu_i^{\mathrm{w}}}{\nu_i^{\mathrm{w}} + \kappa_i \nu_i^{\mathrm{dry}}}. \tag{3.8}$$

For an aerosol particle containing several non-water species, the κ_i for the particle is the volume-weighted mean of the individual κ^a of each species a summed over all non-water species is:

$$\kappa_i = \sum_{a=1}^{A-1} \kappa^a \frac{\nu_i^a}{\nu_i^{\mathrm{dry}}}, \tag{3.9}$$

where $\kappa = 0.65$ for all salts formed from the NH_4^+-SO_4^2-NO_3^- system from (*Petters and Kreidenweis*, 2007) and (*Riemer et al.*, 2010), $\kappa = 0.1$ for secondary organic aerosol in the MOSAIC model based on measurements by (*Prenni et al.*, 2007), $\kappa = 0.001$ for primary organic aerosol, and $\kappa = 0$ for black carbon folowing (*Petters et al.*, 2006).

The rate of change of the environmental saturation ratio, $\dot{S}_{\mathrm{v}}$, is given by

$$\dot{S}_{\mathrm{v}} = -\sum_{i=1}^{N_{\mathrm{p}}} \frac{\pi \rho_{\mathrm{w}} RT}{2 M_{\mathrm{w}} P^0 V_{\mathrm{comp}}} D_i^2 \dot{D}_i - \frac{1}{P^0} \frac{\partial P^0}{\partial T} S_{\mathrm{v}} \dot{T} + S_{\mathrm{v}} \frac{\dot{p}}{p} + \lambda_{\mathrm{entrain}} S_{\mathrm{v}} \frac{(V_{\mathrm{comp}} \rho_{\mathrm{v,back}} - m_{\mathrm{v}})}{m_{\mathrm{v}}}, \tag{3.10}$$

where M_{v} is the mass of water vapor, $\rho_{\mathrm{v,back}}$ is the density of water vapor in the background

3.3 Adding entrainment of Non-Cloudy Air

From the cloud-resolving simulations by Lasher-Trapp (personal communication, 2012), we obtained temporal profiles of total specific humidity, q_{tot}, temperature, T, and pressure, p. Now that we consider entrainment, the total water content of the parcel is not conserved. Mathematically, q_{tot} is as follows:

$$q_{\text{tot}} = \frac{m_{\text{v}}}{(m_{\text{d}} + m_{\text{v}})}, \tag{3.11}$$

where m_{v} is the mass of water vapor and m_{d} is the mass of dry air.

Using the q_{tot} profiles, we derived an entrainment fraction, λ_{entrain} to describe how the liquid water content of the cloud parcel changes. The entrainment fraction is needed to solve equations 3.3 and 3.4. Here we describe how to obtain λ_{entrain} from know quantities. Within a certain volume of air, V_{comp}, the proportion exchanged with background is $\gamma = \lambda \Delta t$, which happens instantaneously. In our notation, we indicate the state before the exchange with "$-$", and the state after the exchange with "$+$". During the entrainment, V_{comp}, T, p of the parcel do not change. We assume that the outside air is sub-saturated and at the same temperature and pressure as the parcel air and that the entrainment of non-cloudy air is homogeneously mixed. The homogeneous assumption is valid becase the turbulent mixing timescale is much larger than the evaporation timescale.

Figure 3.1 shows an example of three-dimensional cloud resolving model data in which we based our inputs for the cloud parcel simulations including the total specific humidity, q and temperature, T. The idealized inputs are as seen in Chapter 5.

3.3.1 Derivation of the Entrainment Fraction

This section derives the entrainment fraction $\gamma = \lambda_{\text{entrain}} \Delta t$. The change in total water mass, m, which includes liquid and vapor, in the parcel due to entrainment is as follows:

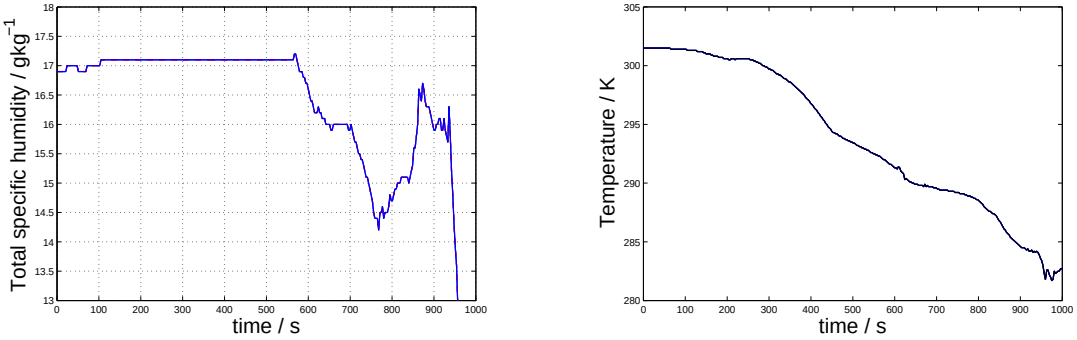

Figure 3.1: Total specific humidity profile (left) and temperature (right) from a 3-D cloud resolving model.

$$\Delta m = m^+ - m^- = \Delta_{\mathrm{G}} m - \Delta_{\mathrm{L}} m. \tag{3.12}$$

The gain in total water mass from background to parcel can be written as:

$$\Delta_{\mathrm{G}} m = \Delta_{\mathrm{G}} m_{\mathrm{l}} + \Delta_{\mathrm{G}} m_{\mathrm{v}} = \gamma V_{\mathrm{comp}} \left(\rho^-_{\mathrm{l,b}} + \rho^-_{\mathrm{v,b}} \right), \tag{3.13}$$

where $m^-_{\mathrm{l,b}}$ is the liquid mass and $m^-_{\mathrm{v,b}}$ is the vapor mass.

The loss of total water mass from parcel to background is:

$$\Delta_{\mathrm{L}} m = \Delta_{\mathrm{L}} m_{\mathrm{l}} + \Delta_{\mathrm{L}} m_{\mathrm{v}} = \gamma \left(m^-_{\mathrm{l}} + m^-_{\mathrm{v}} \right), \tag{3.14}$$

where the liquid mass m^-_{l} and the vapor mass is m^-_{v}.

To obtain the change in total water mass, we took the difference between the gain of total water mass and the loss. This gives:

$$\Delta m = m^+ - m^- = \gamma \left(V_{\mathrm{comp}} \left(\rho^-_{\mathrm{l,b}} + \rho^-_{\mathrm{v,b}} \right) - \left(m^-_{\mathrm{l}} + m^-_{\mathrm{v}} \right) \right). \tag{3.15}$$

Then, Equation (3.15) was divided by the mass of moist air of the parcel before exchange,

$m^-_{\mathrm{air,wet}}$, which is equivalent to $V_{\mathrm{comp}}\rho^-_{\mathrm{air,wet}}$.

$$\frac{\Delta m}{m^-_{\mathrm{air,wet}}} = \frac{m^+}{m^-_{\mathrm{air,wet}}} - \frac{m^-}{m^-_{\mathrm{air,wet}}} = \gamma\left(\frac{\rho^-_{\mathrm{l,b}} + \rho^-_{\mathrm{v,b}}}{\rho^-_{\mathrm{air,wet}}} - \frac{m^-_{\mathrm{l}} + m^-_{\mathrm{v}}}{m^-_{\mathrm{air,wet}}}\right) \tag{3.16}$$

$$\frac{m^+}{m^-_{\mathrm{air,wet}}} - q^-_{\mathrm{tot}} = \gamma\left(q^-_{\mathrm{l,b}} + q^-_{\mathrm{v,b}} - q_{\mathrm{tot}}-\right). \tag{3.17}$$

The first term of Equation (3.17) was rearranged to be in terms of specific humidity:

$$\frac{m^+}{m^-_{\mathrm{air,wet}}} = \frac{m^+}{m^+_{\mathrm{air,wet}}}\frac{m^+_{\mathrm{air,wet}}}{m^-_{\mathrm{air,wet}}} = q^+_{\mathrm{tot}}\frac{m^+_{\mathrm{air,wet}}}{m^-_{\mathrm{air,wet}}} \tag{3.18}$$

$$m^+_{\mathrm{air,wet}} = m^-_{\mathrm{air,wet}} - \Delta_{\mathrm{L}}m_{\mathrm{v}} + \Delta_{\mathrm{G}}m_{\mathrm{v}} \tag{3.19}$$

$$m^+_{\mathrm{air,wet}} = m^-_{\mathrm{air,wet}} + \gamma\left(V_{\mathrm{comp}}\rho^-_{\mathrm{v,b}} - m^-_{\mathrm{v}}\right) \tag{3.20}$$

$$\frac{m^+}{m^-_{\mathrm{air,wet}}} = 1 + \gamma\left(\frac{\rho^-_{\mathrm{v,b}}}{\rho^-_{\mathrm{air,wet}}} - q^-_{\mathrm{v}}\right). \tag{3.21}$$

This new expression replaced the first term in Equation (3.17). We solved for γ, which is an expression for the entrainment fraction.

$$q^+_{\mathrm{tot}}\left(1 + \gamma\left(\frac{\rho^-_{\mathrm{v,b}}}{\rho^-_{\mathrm{air,wet}}} - q^-_{\mathrm{v}}\right)\right) - q^-_{\mathrm{tot}} = \gamma\left(q^-_{\mathrm{tot,b}} - q^-_{\mathrm{tot}}\right) \tag{3.22}$$

$$\gamma = \frac{q^+_{\mathrm{tot}} - q^-_{\mathrm{tot}}}{q^-_{\mathrm{tot,b}} - q^-_{\mathrm{tot}} - q^+_{\mathrm{tot}}\left(\frac{\rho^-_{\mathrm{v,b}}}{\rho^-_{\mathrm{air,wet}}} - q^-_{\mathrm{v}}\right)}. \tag{3.23}$$

If temperature and pressure of background and parcel are similar, we can approximate the fraction $\rho^-_{\mathrm{v,b}}/\rho^-_{\mathrm{air,wet}}$ by:

$$\frac{\rho^-_{\mathrm{v,b}}}{\rho^-_{\mathrm{air,wet}}} = \frac{p_{\mathrm{b}}T\left(1 + \left(\frac{1}{\epsilon} - 1\right)q^-_{\mathrm{v}}\right)}{pT_{\mathrm{b}}\left(1 - q^-_{\mathrm{b}}\right)} \approx \frac{\left(1 + \left(\frac{1}{\epsilon} - 1\right)q^-_{\mathrm{v}}\right)}{\left(1 - q^-_{\mathrm{b}}\right)} \tag{3.24}$$

$$\epsilon = \frac{M_{\mathrm{w}}}{M_{\mathrm{air,dry}}}. \tag{3.25}$$

Using our prescribed q_{tot} profiles, we can determine the entrainment fraction as described in Equation (3.23). During the entrainment event, gases and particles in the cloud parcel are exchanged with the background. This changes the aerosol population in the parcel and the liquid water content of the parcel, so the notation of q_{l}^{-} is changed to $q_{\text{l,new}}^{-}$. The updated value $q_{\text{l,new}}^{-}$ is then used to update the parcel relative humidity, so that the prescribed q_{tot}^{-} is matched. The new saturation ratio, S_{v} is described as follows:

$$q_{\text{v,new}}^{-} = q_{\text{tot}}^{-} - q_{\text{l,new}}^{-} \tag{3.26}$$

$$p_{\text{v,new}}^{-} = \frac{q_{\text{v,new}}^{-} p}{\epsilon + q_{\text{v,new}}^{-}(1-\epsilon)} \tag{3.27}$$

$$S_{\text{v,new}^{-}} = \frac{p_{\text{v,new}}^{-}}{P^{0}(T)}, \tag{3.28}$$

where $\epsilon = \frac{M_{\text{w}}}{M_{\text{air}}}$.

3.4 Constructing Initial Conditions

The initial conditions of the cloud parcel simulation need to be consistent with with our prescribed q_{tot} profiles. To do so, we calculated the initial saturation ratio, S_{v}, from the input variables of initial temperature, T, pressure, p, and specific humidity, $q_{\text{tot,init}}$. The following shows the derivation of S_{v}. First, we derived an equation for the density of water vapor, ρ_{v}, in terms of these initial inputs.

We start with four initial equations:

$$\rho_{\mathrm{v}} = \frac{\rho_{\mathrm{d}} q_{\mathrm{tot,init}} - \rho_{\mathrm{l}}}{1 - q_{\mathrm{tot,init}}} \tag{3.29}$$

$$\rho_{\mathrm{air,wet}} = \frac{p}{R_{\mathrm{d}} T (1 + c q_{\mathrm{v}})} \tag{3.30}$$

$$\rho_{\mathrm{d}} = \rho_{\mathrm{air,wet}} - \rho_{\mathrm{v}} \tag{3.31}$$

$$q_{\mathrm{v}} = \frac{\rho_{\mathrm{v}}}{\rho_{\mathrm{air,wet}}}. \tag{3.32}$$

Plugging (3.32) into (3.30), we eliminate q_{v}

$$\rho_{\mathrm{air,wet}} = \frac{p}{R_{\mathrm{d}} T (1 + c \frac{\rho_{\mathrm{v}}}{\rho_{\mathrm{air,wet}}})} \tag{3.33}$$

$$\rho_{\mathrm{air,wet}} = \frac{p}{R_{\mathrm{d}} T (\frac{\rho_{\mathrm{air,wet}} + c\rho_{\mathrm{v}}}{\rho_{\mathrm{air,wet}}})} \tag{3.34}$$

$$\rho_{\mathrm{air,wet}} = \frac{\rho_{\mathrm{air,wet}} p}{R_{\mathrm{d}} T (\rho_{\mathrm{air,wet}} + c\rho_{\mathrm{v}})} \tag{3.35}$$

$$R_{\mathrm{d}} T (\rho_{\mathrm{air,wet}} + c\rho_{\mathrm{v}}) \rho_{\mathrm{air,wet}} = \rho_{\mathrm{air,wet}} p \tag{3.36}$$

$$R_{\mathrm{d}} T \rho_{\mathrm{air,wet}}^2 + R_{\mathrm{d}} T c \rho_{\mathrm{v}} \rho_{\mathrm{air,wet}} - \rho_{\mathrm{air,wet}} p = 0 \tag{3.37}$$

$$\rho_{\mathrm{air,wet}} = \frac{p - R_{\mathrm{d}} T c \rho_{\mathrm{v}}}{R_{\mathrm{d}} T}. \tag{3.38}$$

Now there are three equations we will use to eliminate ρ_{d} and ρ:

$$\rho_{\mathrm{v}} = \frac{\rho_{\mathrm{d}} q_{\mathrm{tot,init}} - \rho_{\mathrm{l}}}{1 - q_{\mathrm{tot,init}}} \tag{3.39}$$

$$\rho = \frac{p - R_{\mathrm{d}} T c \rho_{\mathrm{v}}}{R_{\mathrm{d}} T} \tag{3.40}$$

$$\rho_{\mathrm{d}} = \rho_{\mathrm{air,wet}} - \rho_{\mathrm{v}}. \tag{3.41}$$

Plugging (3.41) into (3.39) to eliminate ρ_{d}:

$$\rho_{\mathrm{v}} = \frac{(p - \rho_{\mathrm{v}})q_{\mathrm{tot,init}} - \rho_{\mathrm{l}}}{1 - q_{\mathrm{tot,init}}} \tag{3.42}$$

$$\rho_{\mathrm{v}}(1 - q_{\mathrm{tot,init}}) = \rho_{\mathrm{air,wet}}q_{\mathrm{tot,init}} - \rho_{\mathrm{v}}q_{\mathrm{tot,init}} - \rho_{\mathrm{l}} \tag{3.43}$$

$$\rho_{\mathrm{v}} = \rho_{\mathrm{air,wet}}q_{\mathrm{tot,init}} - \rho_{\mathrm{l}} \tag{3.44}$$

$$\rho_{\mathrm{air,wet}} = \frac{p - R_{\mathrm{d}}T_{\mathrm{c}}\rho_{\mathrm{v}}}{R_{\mathrm{d}}T}. \tag{3.45}$$

Plugging (3.41) into (3.44) to eliminate ρ:

$$\rho_{\mathrm{v}} = \frac{p - R_{\mathrm{d}}Tc\rho_{\mathrm{v}}}{R_{\mathrm{d}}T}q_{\mathrm{tot,init}} - \rho_{\mathrm{l}} \tag{3.46}$$

$$\rho_{\mathrm{v}} = \frac{pq_{\mathrm{tot,init}} - \rho_{\mathrm{l}}R_{\mathrm{d}}T}{R_{\mathrm{d}}T + R_{\mathrm{d}}Tcq_{\mathrm{tot,init}}}. \tag{3.47}$$

Now the vapor pressure $e = \rho_{\mathrm{v}}R_{\mathrm{v}}T$ can now be described as:

$$e = \frac{pq_{\mathrm{tot,init}} - \rho_{\mathrm{l}}R_{\mathrm{d}}T}{R_{\mathrm{d}}T + R_{\mathrm{d}}Tcq_{\mathrm{tot,init}}}R_{\mathrm{v}}T \tag{3.48}$$

$$R_{\mathrm{v}} = \frac{R^*}{m_{\mathrm{w}}}, R_{\mathrm{d}} = \frac{R^*}{m_{\mathrm{d}}}, c = \frac{1}{\epsilon} - 1, \epsilon = \frac{m_{\mathrm{w}}}{m_{\mathrm{d}}}. \tag{3.49}$$

The equation for saturation vapor pressure $P^0(T)$ is as follows:

$$P^0(T) = 611.2 \exp\left(7.45 \ln(10)\frac{T - 273.15}{T - 38}\right). \tag{3.50}$$

$$\tag{3.51}$$

The new saturation ratio, S_{v}, can be solved using:

$$S_{\mathrm{v}} = \frac{e}{P^0(T)}. \tag{3.52}$$

A preprocessing routine is run for 600 seconds with no equilibriation so that the S_{v} can adjust according to the present particle population. The S_{v} from end of this pre-processing routine is the initial S_{v} for our simulations.

Chapter 4

Urban Plume Simulation

A Langrangian air parcel moved over a polluted urban environment. Then, we took the aerosol populations at selected hours to initialize the cloud parcel model. Here we summarize the urban plume scenario as described in *Zaveri et al.* (2010).

4.1 Simulation Setup

The simulation was run with 10,000 computational particles for 24 hours, with a 1 hour timestep and begins as an air parcel is advected within the mixed layer over a large urban area. The parcel contains background air composed of 50 ppbv O_3 and other trace gases, as well as ammonium sulfate internally mixed with SOA and trace amounts of black carbon. For the first 12 hours of simulation starting at 0600 local standard time (LST), the parcel experiences continous emissions of NO_x, SO_2, CO, volatile organic compounds (VOCs), and three types of primary aerosol particles. These include diesel soot (70% BC and 30% primary organic aerosol (POA)), gasoline soot (20% BC and 80% POA), and meat cooking primary organic aerosol (100% POA). We modeled a well-mixed boundary layer during the day and a residual layer during the night, both of which are surrounded by background air containing prescribed gases and aerosols. There is dilution with the background air as the boundary

layer grows during the simulation, as well as dilution with the background. After the first 12 hours of simulation, the parcel leaves the urban area and no emissions are present. A stable boundary layer develops during the night and is decoupled from the polluted residual layer. We use the particle populations from plume hour 1, 12 and 24 h after the start of the simulation, which are referred to as the plume time, t_{plume}. Particle populations from these three times are used to initalize the cloud parcel model. Hour 1 represents fresh emissions, while hour 12 and 24 respresent an aged population. Since emission are only operating for the first 12 hours, plume hour 12 and 24 show different degrees of aging, which will be evident in section 4.2.

4.2 Simulation Results

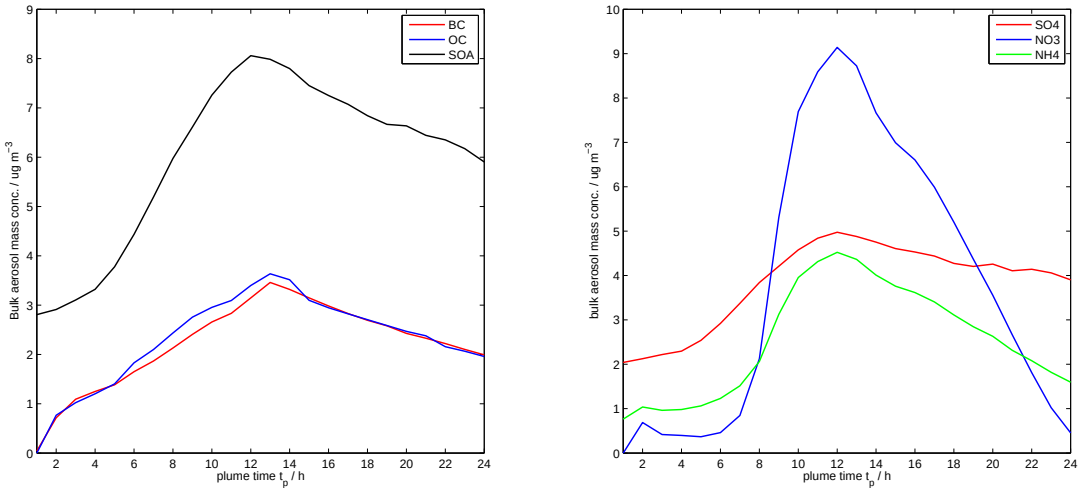

Figure 4.1: Evolution of the bulk aerosol mass concentration.

The bulk aerosol mass concentration are shown in Figure 4.1. The BC and OC concentrations increased for the first 12 hours due to emissions. At 12 hours, the emissions are turned off at which point the concentrations began to decrease due to dilution with the background.

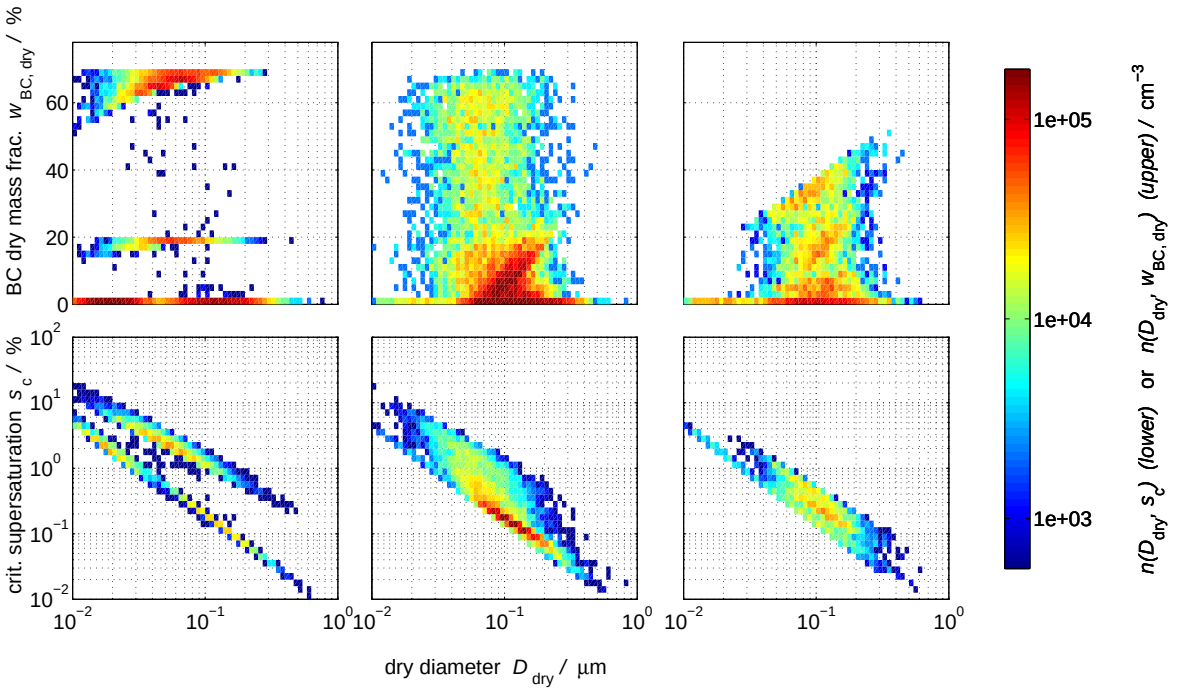

Figure 4.2: Two-dimensional number concentration distribution $n(D_{\mathrm{dry}},\ w_{\mathrm{BC,dry}})$ at $t_p = 1, 12, 24$ h shown in the top panels and the critical supersaturation, $n(D_{\mathrm{dry}}, s_c)$ shown in the bottom panels.

The BC mass fraction in particle i describes the BC mixing state as follows:

$$w_{\mathrm{BC,dry},i} = \frac{\mu_i^{\mathrm{BC}}}{\mu_i^{\mathrm{dry}}} \tag{4.1}$$

where μ_i^{BC} is the mass of BC in particle i and μ_i^{dry} is the total dry mass of the particle. The two-dimensional number concentration $n(d, w)$ is defined as:

$$n(D, w) = \frac{\partial^2 N(D, w)}{\partial log_{10} D \partial w} \tag{4.2}$$

Figure 4.2 shows the two-dimensional number concentration distribution of the particles as a function of dry diameter and BC dry mass fraction, $n(D_{\mathrm{dry}})$, $w_{\mathrm{BC,dry}}$ after simulating for 1, 12, and 24 hours. Three particle types due to fresh emissions can be seen. At $t_p = 1$,

$w_{\mathrm{BC,dry}} = 0\%$ for background particles and cooking emissions, $w_{\mathrm{BC,dry}} = 20\%$ for gasoline vehicle emissions, and $w_{\mathrm{BC,dry}} = 70\%$ for diesel vehicle emissions. Particles that exist at other values of $w_{\mathrm{BC,dry}}$ have coagulated with particles of a different major source catergory or SOA condensed onto the particles, thus altering the BC dry mass fraction. At t_{plume} =12 h, the fresh particles coexist with the particles that have aged via condensation and coagulation. At this point, emissions are turned off. By t_{plume} =24 h, the BC mass fraction has lowered and the particle population has shifted to larger sizes. The smaller particles were lost through coagulation. Throughout the simulation, small background particles enter the plume through dilution. Also shown in Figure 4.2, is the number concentration as a function of the dry diameter and critical supersaturation, $n(D_{\mathrm{dry}}, s_{\mathrm{c}})$. The size and composition determine the critical supersaturation. The larger particles have a lower critical supersaturation, agreeing with Köhler theory. At one size, there is also a spread in the critical supersaturation, which is due to the different particle compositions. The critical supersaturation gradually decreases with time since the aged particles have increased in hygroscopicity. The spread in s_{c} narrows by hour 24 after emissions are turned off and the population becomes more internally mixed.

Chapter 5

Cloud Parcel Simulation

In this section, we compare idealized cloud parcel simulations with entrainment to simulations without entrainment. We aim to test the new model capability and investigate how the black carbon mixing state impacts cloud microphysical properties and nucleation-scavenging of black carbon particles when entrainment is included. All cloud parcel simulations are performed according to the following setup. The particle populations from the three plume hours in Figure 4.2 are used to initialize the cloud parcel. The simulations ran for 1000 s with a 1 s timestep, and we refer to this as the parcel time, t_{parcel}. During a cloud parcel run, we prescribe temperature T, pressure, P, and total specific humidity, q. We prescribe the background particles and the air surrounding the cloud parcel to be at the same T and p as the parcel. The only processes occuring in the cloud parcel are evaporation and condensation of water vapor, and entrainment. During an entrainment event, subsaturated air is homogeneously exchanged with the cloud parcel, which changes the aerosol and cloud droplet population. Three cases are presented in this thesis. Case 1 uses an idealized Q profiles, idealized constant cooling rates, and a constant pressure profile. Case 1 has similar inputs to *Ching et al.* (2012), but now includes entrainment. Case 2 uses idealized q profiles and less idealized T and p profiles as inputs that were constucted from high-resolution three-dimensional cloud simulation data. Case 3 uses composition averaged particle populations to initialize the cloud parcel, which are compared to the reference case (Case 2).

This is done to investigate the impacts of mixing state on cloud micophysical properties and black carbon-nucleation scavenging. The entrainment process is modeled as stochastic so an ensemble of cloud parcel simulations were simulated. The results presented here have an average of a 10 member ensemble with 95% confidence intervals unless otherwise noted.

5.1 Case 1: Simulation Setup

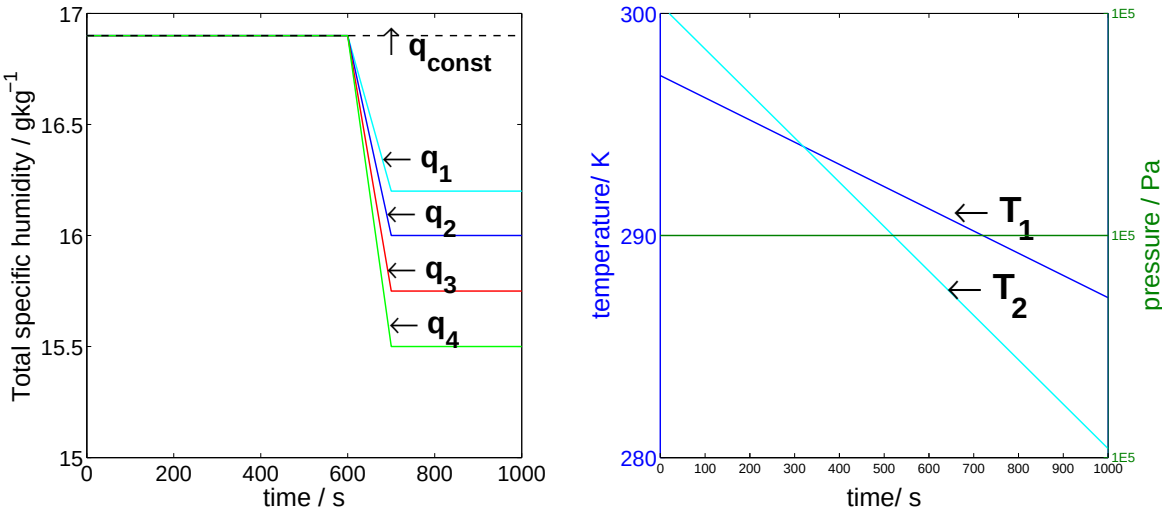

Figure 5.1: Inputs for Case 1 including the total specific humidity profile, q (left), temperature, T, and pressure, p (right).

The inputs for Case 1 are seen in Figure 5.1. We performed runs for five different total specific humidty profiles, q_{const}, q_1, q_2, q_3, q_4, where q represents no entrainment, q_1 represents the smallest amount of entrainment and q_4 represents the largest amount. For each plume hour, q, q_1, q_2, q_3, and q_4 were compared with two cooling rates of 0.01 K/s and 0.02 K/s for T_1 and T_2 respectively. We used the particle populations from t_{plume}=1, 12, and 24 hours from Figure 4.2 as input into the cloud parcel simulations. We compare 5 q profiles with 2 T profiles and 3 plume hours, for a total of 30 scenarios in Case 1. For this case, we compare the effects the entrainment on the cloud microphysical properties including relative humidity (RH), liquid water content (LWC), cloud droplet number concentration (CDNC),

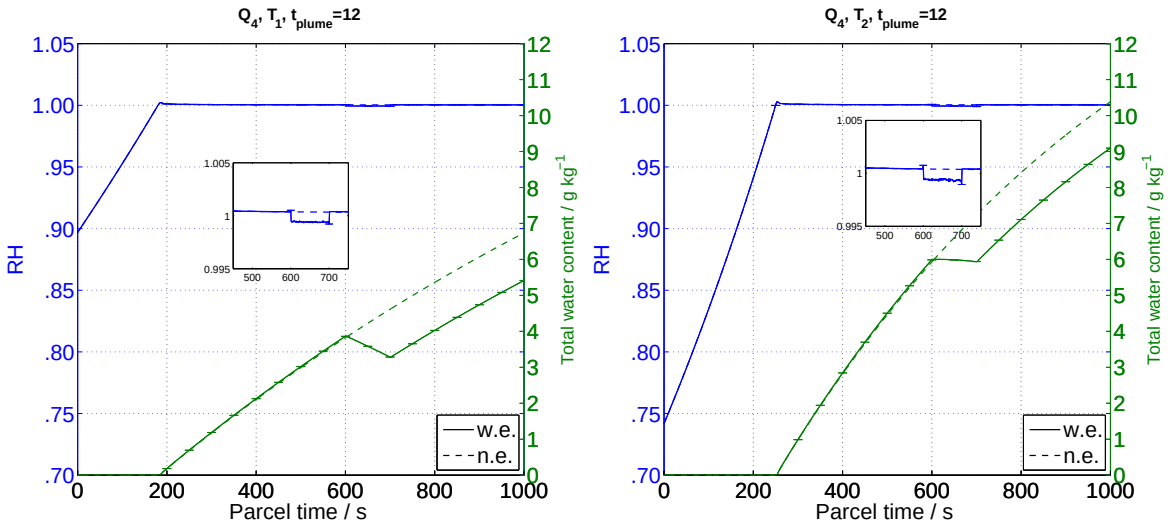

Figure 5.2: Relative humidity and total water content profile for q_4, T_1 (left) and q_4, T_1 for $t_{\text{plume}} = 12$ h (right)

maximum supersaturation in section 5.1.1, and the number concentration size distribution in section 5.1.2.

5.1.1 Results: Impact of Entrainment of Bulk Cloud Properties

Figure 5.2 shows the time series of relative humidity and total water content for cases q_4, T_1, and t_{plume}=12 h and q_4, T_2, and t_{plume}=12 h with the dotted lines representing no entrainment and the solid lines represent with entrainment. We chose $t_{\text{plume}} = 12$ h to show a population that consists of aged particles along with freshlt emitted particles. In Figure 5.2, we use largest amount of entrainment, q_4, to show the most extreme conditions. Without entrainment, the RH profile increases as a result of the prescribed cooling rate and the loss of water vapor due to condensation on the particles according to equation 3.10. This is similar to what is shown in *Ching et al.* (2012). The droplets activate and the critical supersaturation was reached around $t_{\text{parcel}} = 190$ s. At this time, the LWC becomes greater than zero and continues to increase during the remaining time of the cloud parcel simulation.

The entrainment event occurs between 600 and 700 s of the simulations, which alters the RH profiles during these times. During the entrainment event, the RH decreases to less

than 100% due to the incorporation of sub-saturated air. When the event is over, the RH increases until the parcel is supersaturated again. The decrease in RH due to entrainment has a similar magnitude for both cooling rates. At 600s, the total water content decreases as well. The liquid water content gradually increases with time for the remaining simulation time. The cloud formed later when using the stronger cooling rate, T_2 and reached a higher LWC than T_1 by the end of the simulation. This difference was due to the lower initial RH and the higher maximum supersaturation of the T_2 profile.

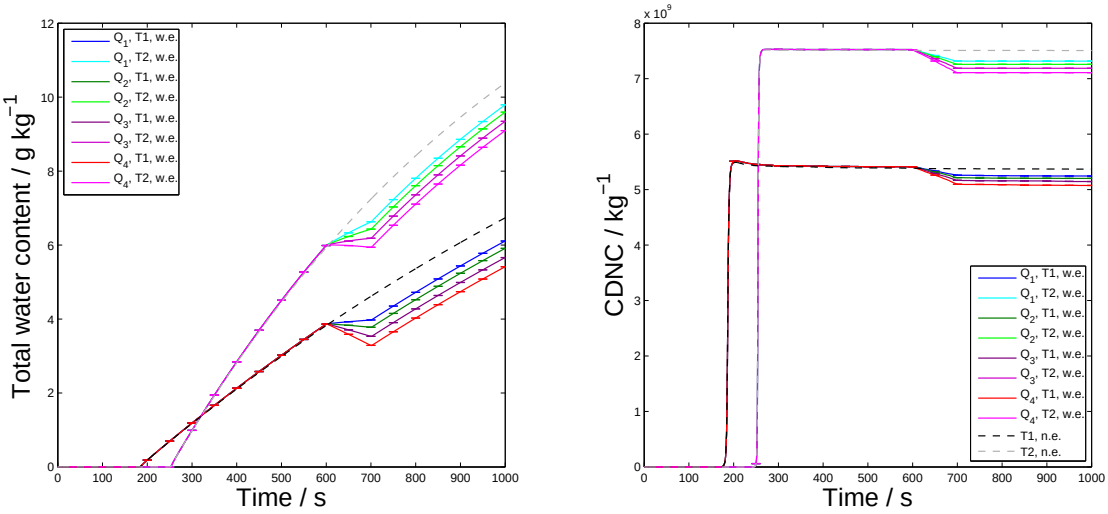

Figure 5.3: Liquid water content (left) and cloud droplet number concentration (right) for all q and T cases using $t_{\text{plume}} = 12$ h.

Next, we compare the impact of the amount of entrainment. Here we look at the LWC and CDNC profiles over the course of the simulation from $t_{\text{plume}} = 12$ h for all q and T profiles. As shown in Figure 5.3, the dotted lines represent the no entrainment cases, and the solid represent with entrainment. The results are as expected, where the smallest entrainment event, q_1, led to the smallest percent decrease in LWC compared with the no entrainment case and the largest event, q_4, led to the largest decrease in LWC. When using T_2 profiles, which represented the larger cooling rate, the cloud formed later than T_1 because the initial RH was lower, but resulted in a larger liquid water content (LWC) after $t_{\text{parcel}} = 300$ s due to a stronger cooling rate. At 1000 seconds, the q_4, T_2, $t_{\text{plume}} = 12$ h scenario and

had a total liquid water content of 9 g kg^{-1} compared to the no entrainment value of 10 g kg^{-1}, resulting in a 10% decrease due to the entrainment. The T_1 profile had a LWC of 5 g kg^{-1}, corresponding to a 20% decrease. The percent difference at the end of the simluation between the strong and weaker cooling rates was 45%.

The cloud droplet number concentration follows the same pattern. The smallest entrainment event, q_1, led to the smallest percent decrease in and CDNC compared with the no entrainment case and the largest event, q_4, led to the largest decrease in CDNC. At the end of the simulation, the CDNC differs by around 4% between q_1 and $q4$. The particles activated earlier with T_1, but less particles activated than when using the stronger cooling rate, T_2. The q_4 profile decreased around 5% from the no entrainment value for case T_1 and T_2. There was a 30% decrease in the CDNC in T_1. The T_2 profiles resulted in higher maximum supersaturation values, allowing for a higher CDNC. The decrease in LWC due to entrainment in our simulation agrees with (*Blyth et al.*, 2005) and *Barahona and Nenes* (2007).

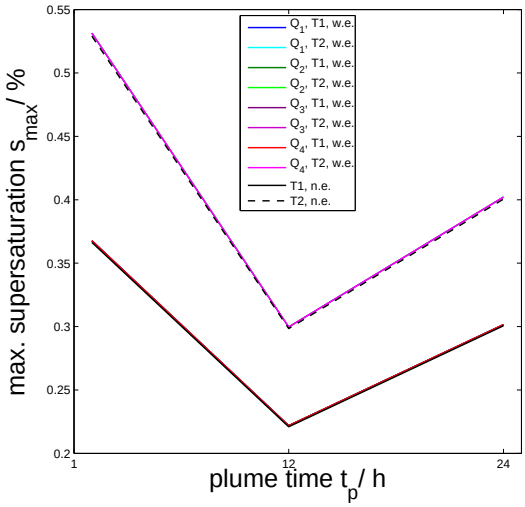

Figure 5.4: Maximum supersaturation from one ensemble member for all scenarios and plume hours.

The effects of aging on cloud droplet activation can be seen by comparing T and q across all plume hours $t_{\text{plume}} = 1, 12, 24$ h. In Figure 5.4, the maximum supersaturation, $s_{\max}$ for all

eight entrainment scenarios and two no entrainment scenarios are plotted against the plume hour. The $s_{\max}$ for the larger cooling rate ranged from 0.52% to .3%, while $s_{\max}$ ranged from 0.37% to 0.22% for T_1. All scenarios with the same cooling had the same $s_{\max}$ for each plume hour because the maximum supersaturation occured before the entrainment events in all cases. The maximum supersaturation was largest for $t_{\text{plume}} = 1$ h and smallest for $t_{\text{plume}} = 12$ h.

5.1.2 Impact of Entrainment on the Size Distribution

Figure 5.5 shows the particle and droplet size distribution as a function of wet diameter, $n(D_{\text{wet}})$ for scenario q_1, $T1$, $t_{\text{plume}} = 1$ h. Solid lines are with entrainment and dashed lines are no entrainment at parcel time t_{parcel} =0 (red), 550 (blue), 650 (green), and 800 (black) seconds. At $t_{\text{parcel}} = 200$s aerosol activation occurred and after this time the distribution is bimodal. The smaller particles are the interstitial aerosols, while the larger particle represent the cloud droplets. Following the setup in *Ching et al.* (2012), particle with wet diameter larger than 2 μm were considered cloud droplets. As the entrainment of non-cloudy air entered the cloud, the droplets partially evaporated and the cloud droplet distribution shifted towards a smaller wet diameter. To emphasize the shift in the cloud droplet distribution to smaller sizes due to entrainment, Figure 5.6 shows the cloud droplet distribution at $t_{\text{parcel}} = 800$ s for the largest amount of entrainment, q_4, the smaller cooling rate, T_1, and the particle population from $t_{\text{plume}} = 12$ h.

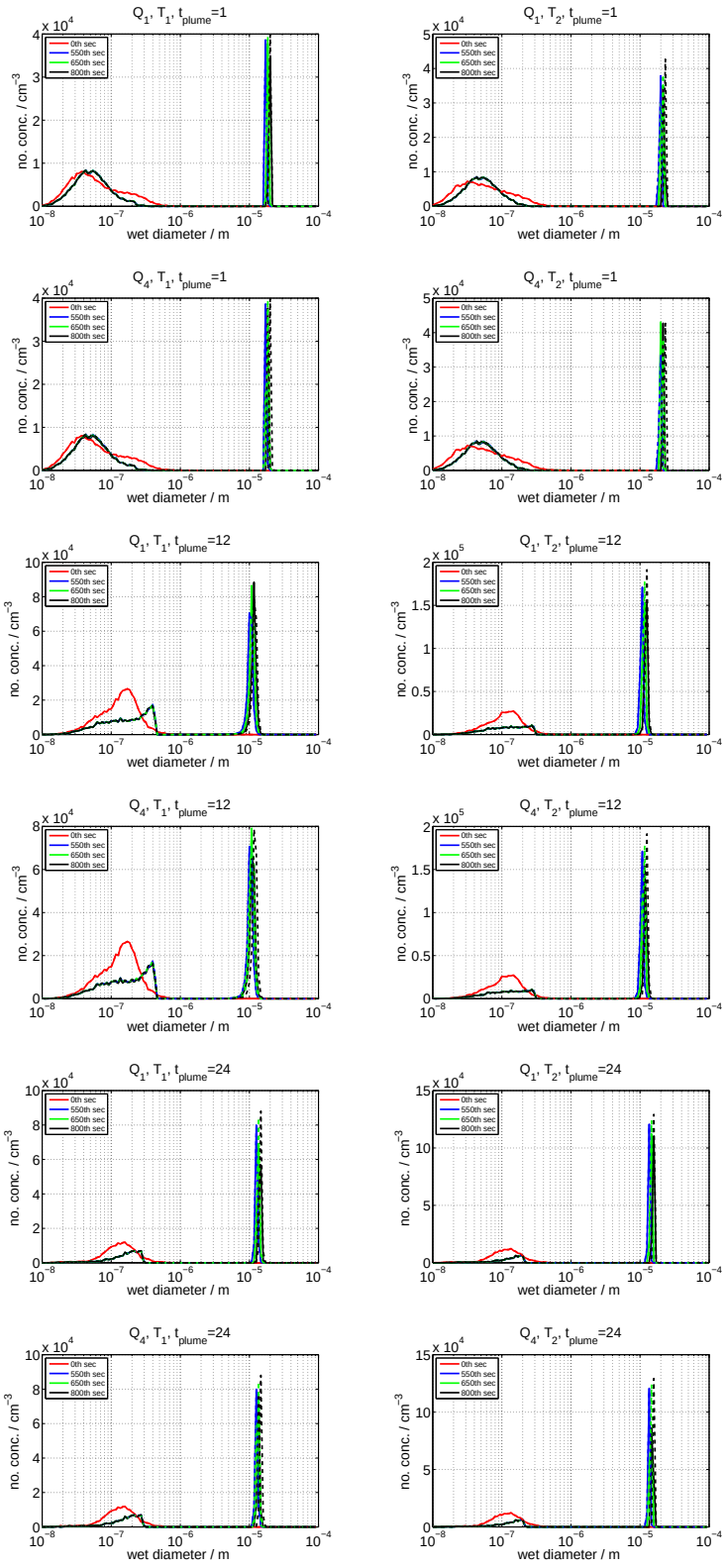

Figure 5.5: Size distributions from one ensemble member based on wet diameter $n(D_{\text{wet}})$. Solid lines are with entrainment and dashed lines are no entrainment at parcel time t_{parcel} =0 (red), 550 (blue), 650 (green), and 800 (black) seconds.

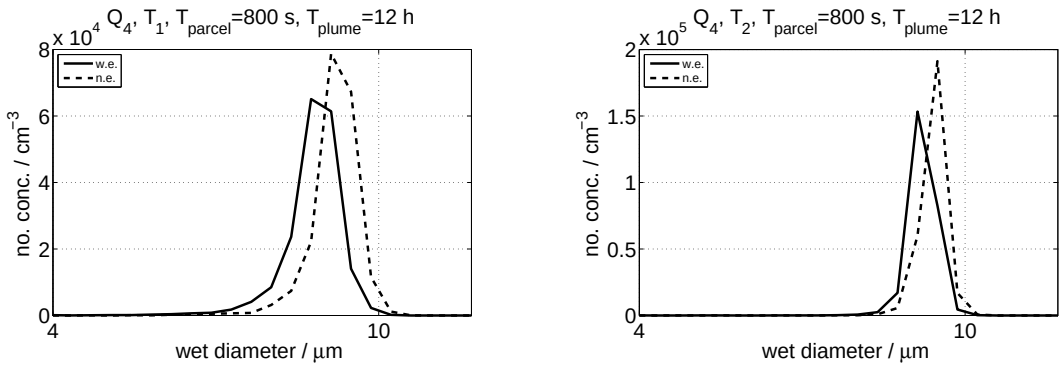

Figure 5.6: Size distributions from one ensemble member based on wet diameter $n(D_{wet})$ for scenario q_4, T_1, $t_{\text{plume}} = 12$ h and q_4, T_2, $t_{\text{plume}} = 12$ h at t_{parcel}=800 s.

Amt. Ent.	T1, w.e.	T1, n.e.	T2, w.e.	T2, n.e.
Q1	0.57	0.24	0.70	0.16
Q2	0.65	0.24	0.91	0.16
Q3	0.74	0.24	1.06	0.16
Q4	0.84	0.24	1.18	0.16
Amt. Ent.	**T1, w.e.**	**T1, n.e.**	**T2, w.e.**	**T2, n.e.**
Q1	1.09	1.04	0.57	0.57
Q2	1.10	1.04	0.57	0.57
Q3	1.13	1.04	0.58	0.57
Q4	1.17	1.04	0.60	0.57
Amt. Ent.	**T1, w.e.**	**T1, n.e.**	**T2, w.e.**	**T1, n.e.2**
Q1	0.52	0.45	0.32	0.26
Q2	0.50	0.45	0.36	0.26
Q3	0.53	0.45	0.35	0.26
Q4	0.53	0.45	0.39	0.26

Figure 5.7: Standard deviations of the size distribution in μm for t_{plume} =1 h in grey, t_{plume} =12 h in blue, and t_{plume}=24 h in red at t_{parcel}=800 s. With entrainment is denoted as w.e. and no entrainment as n.e.

To compare the size distribution with entrainment for all scenarios to the no entrainment scenarios, the standard deviations for plume hour 1, 12, and 24 at t_{parcel}=800 s were calculated and are listed in Figure 5.7. No variations took place in the no entrainment cases with the same cooling rate and plume hour. The standard deviation was greater for entrainment cases compared to the no entrainment case with same temperature profile, except q_1, T_2, t_{plume}=12 h and q_2, T_2, t_{plume}=12 h, in which the standard deviation was less than the no entrainment standard deviation and equal than the no entrainment standard deviation, respectively.

5.2 Case 2

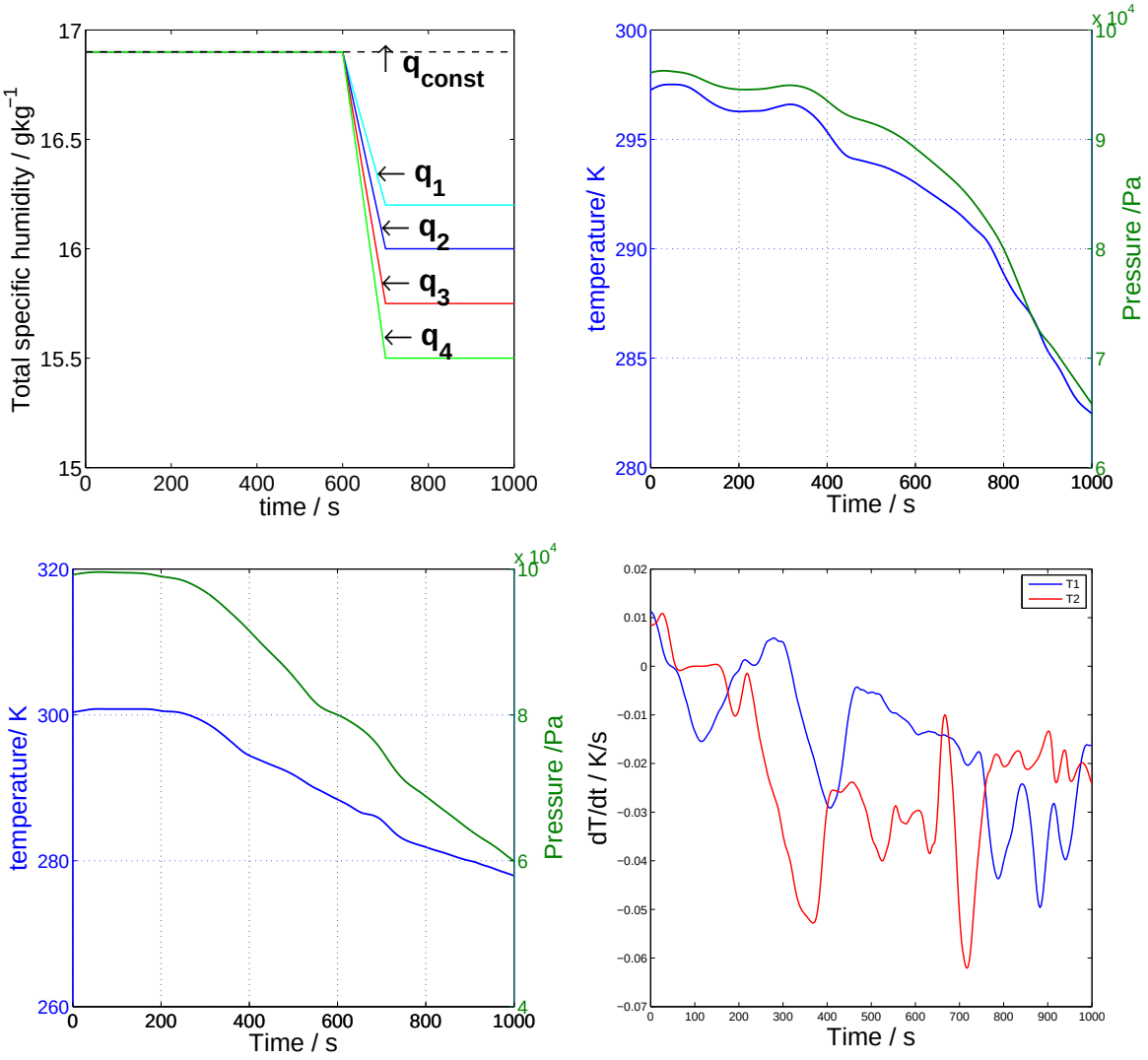

Figure 5.8: Inputs for Case 2 including total specific humidity, q (left, top), temperature and pressure, T_1, P_1 (right, top), temperature and pressure, T_2, P_2 (left, bottom, and the change in temperature over cloud parcel time, dT/dt in K/s (right, bottom).

The inputs for Case 2 are seen in Figure 5.8. The idealized q profiles, two temperature and pressure profiles, and the change in temperature with time for T_1 and T_2 are shown.

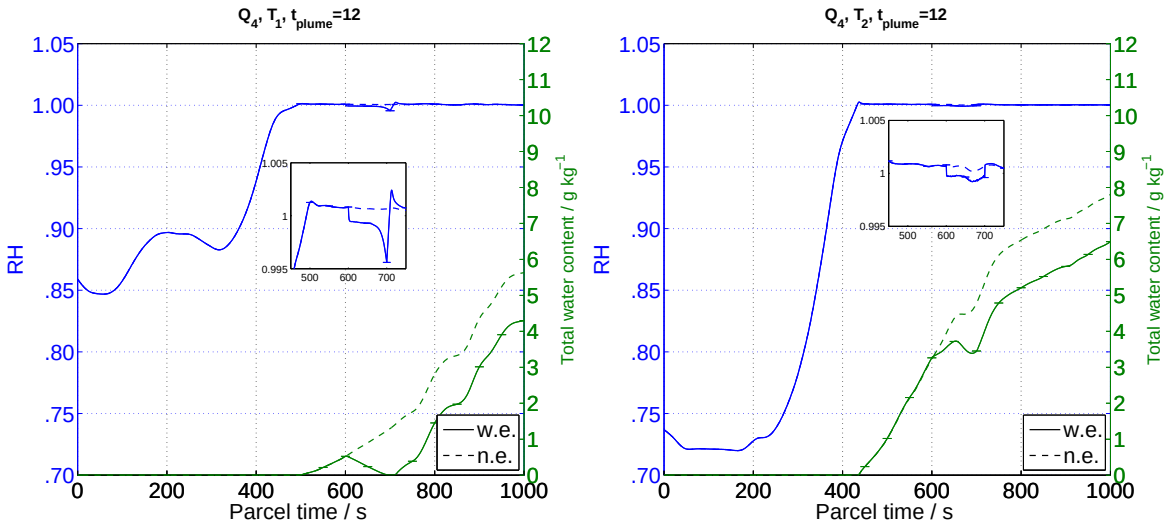

Figure 5.9: Relative humidity for q_4, T_1, $t_{\text{plume}} = 12$ h (left) and q_4, T_2, $t_{\text{plume}} = 12$ h (right).

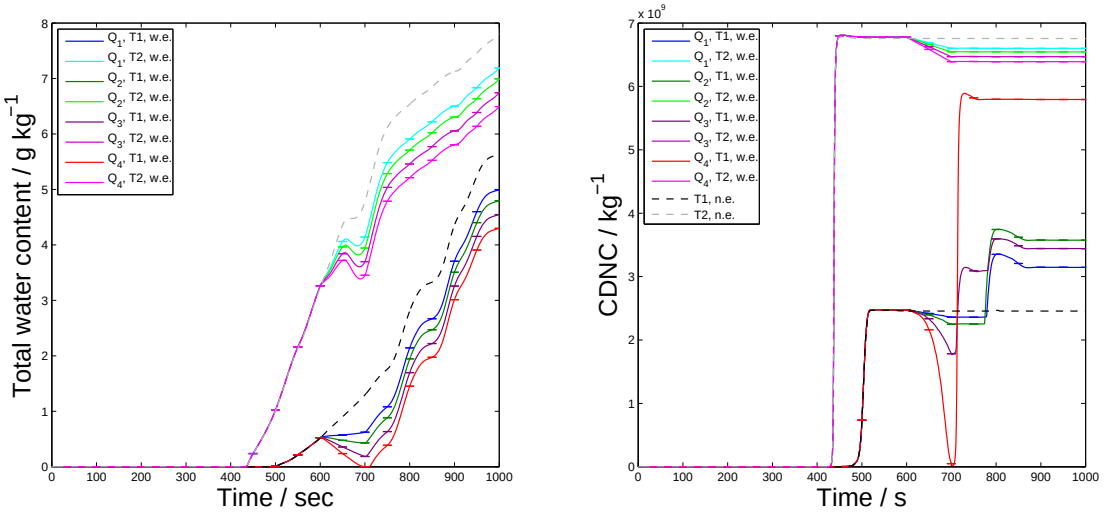

Figure 5.10: Liquid water content (left) and the cloud droplet number concentration (right) for all scenarios.

5.2.1 Impact of Entrainment on Bulk Cloud Properties

In Figure 5.9, the entrainment event for q_4, T_1, $t_{\text{plume}} = 12$ h caused a larger decrease in the RH profile than Case 1. In this scenario, the RH decreased to around 99.6%. As soon as the entrainment event ended, the parcel became supersaturated again. This large drop in RH evaporated the cloud droplets, and the droplets reactivated at a higher supersaturation than the first time. When using T_2 profiles, a higher LWC was reached so the decrease due

to entrainment did not fully evaporate the cloud droplets. The large decrease in RH can be explained by the variablity in the temperature profile. The cooling rates varied between -0.06 and 0.01 K/s throughout the simulation, causing more variance in the cloud properties. This caused the CDNC to be higher than the no entrainment value as seen when using T_1 profiles. For scenarios using T_2 profiles, the CDNC decreased below the no entrainment value as expected. For the scenario q_4, T_1, $t_{\text{plume}} = 12$ h, the cloud evaporated and hygroscopic background particles replaced the cloud droplets. This allowed for a larger amount of particles to activate than the smaller entrainment events. Figure 5.11 shows the maximum supersaturation, which follows the same pattern as Case 1 for the temporal evolution. Entrainment scenarios matched the no entrainment scenario when using T_2 profiles, since the maximum supersaturation occured before the entrainment event. Follwing the pattern in the CDNC, T_2 has a higher supersaturation allowing more droplets to activate than T_1. When using T_1 scenarios, a larger supersaturation was reached when including entrainment compared to not including entrainment during the simulation. The largest entrainment event, q_4 was 0.15% greater than the no entrainment scenario for $t_{\text{plume}} = 1$ h.

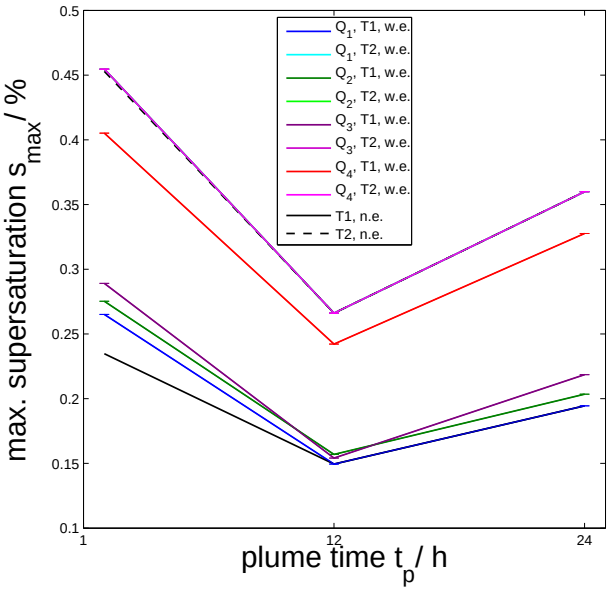

Figure 5.11: Maximum supersaturation for all scenarios.

5.2.2 Impact of Entrainment on the Size Distribution

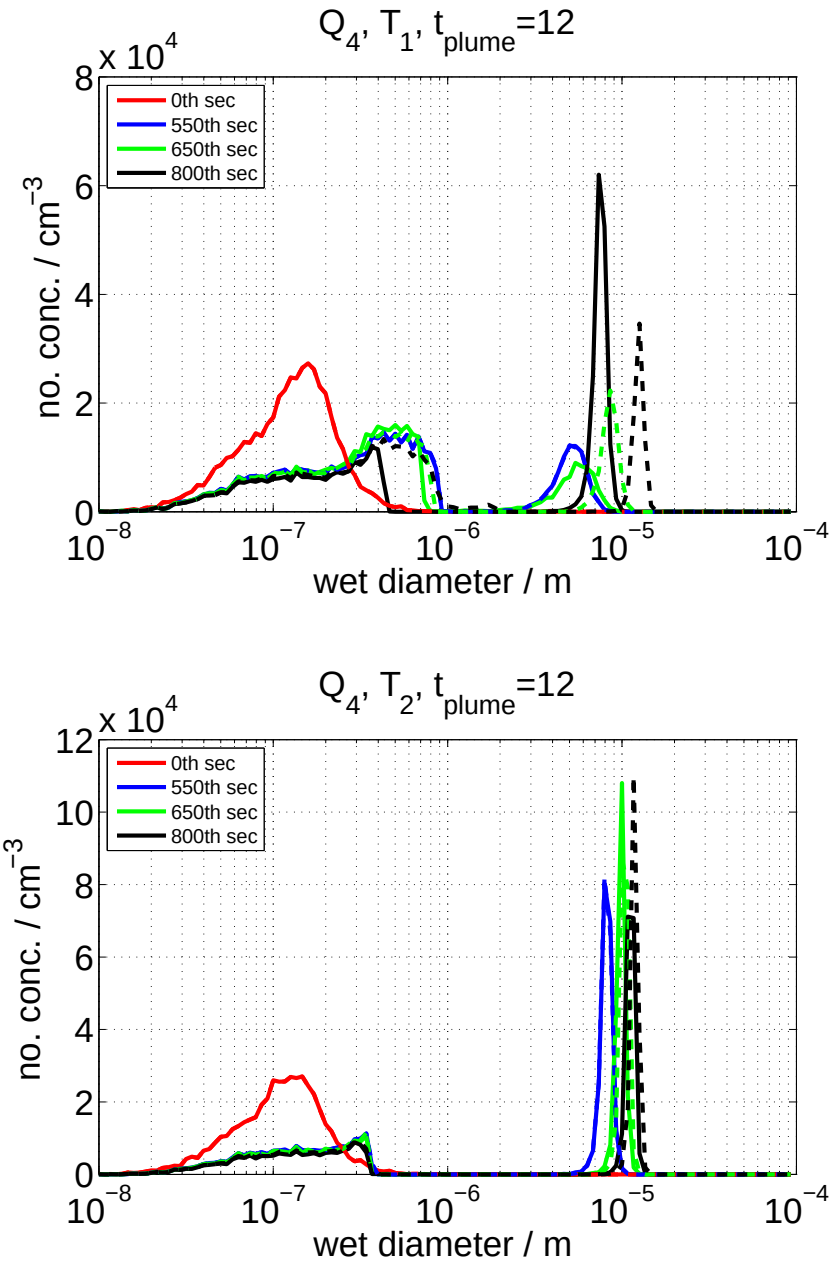

Figure 5.12: Average size distributions from one ensemble member based on wet diameter $n(D_{\text{wet}})$ for parcel time t_{parcel} =0 (red), 550 (blue) 650 (green) and 800 (black) seconds.

Figure 5.12 shows the average size distributions from one ensemble member as in Case 1. The size distribution shows a broadening due to entrainment similar to Case 1. Figure 5.13 shows the broadening in the distribution for when t_{parcel} =800 s. For example, the entrainment case for q_4, T_2,t_{plume} = 12 h has a standard deviation of $\sigma = 0.65$ μm and the no entrainment case has $\sigma = 0.6$ μm. The standard deviations for all scenario are seen in Figure 5.14. Our results are unique in that when calculating growth by condensation, the particle-resolved distributions do not suffer from numerical diffusion.

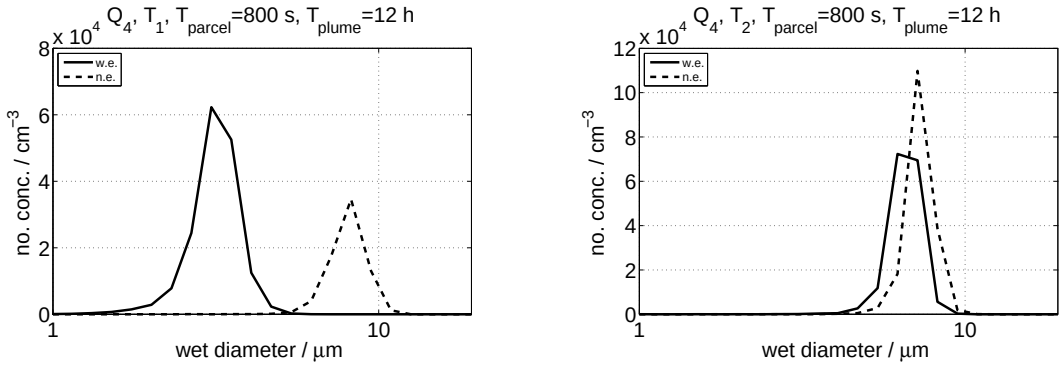

Figure 5.13: Size distributions from one ensemble member based on wet diameter $n(D_{wet})$ for scenario q_4, T_1, $t_{\text{plume}} = 1$ h. The solid line is with entrainment and the dotted line is no entrainment at parcel time $t_{\text{parcel}} = 800$ seconds.

Amt. Ent.	T1, w.e.	T1, n.e.	T2, w.e.	T2, n.e.
Q1	3.71	3.81	1.43	0.18
Q2	3.50	3.81	1.69	0.18
Q3	3.02	3.81	1.81	0.18
Q4	0.31	3.81	1.99	0.18
Amt. Ent.	**T1, w.e.**	**T1, n.e.**	**T2, w.e.**	**T2, n.e.**
Q1	3.97	0.85	0.63	0.60
Q2	3.88	0.85	0.63	0.60
Q3	2.89	0.85	0.64	0.60
Q4	0.71	0.85	0.65	0.60
Amt. Ent.	**T1, w.e.**	**T1, n.e.**	**T2, w.e.**	**T1, n.e.2**
Q1	3.20	0.56	0.40	0.29
Q2	3.51	0.56	0.47	0.29
Q3	3.56	0.56	0.55	0.29
Q4	0.44	0.56	0.64	0.29

Figure 5.14: Standard deviations of the size distribution in μm for t_{plume} =1 h in grey, t_{plume} =12 h in blue, and t_{plume}=24 h in red at t_{parcel}=800 s. With entrainment is denoted as w.e. and no entrainment as n.e.

5.3 Case 3: Composition Averaged Simulation

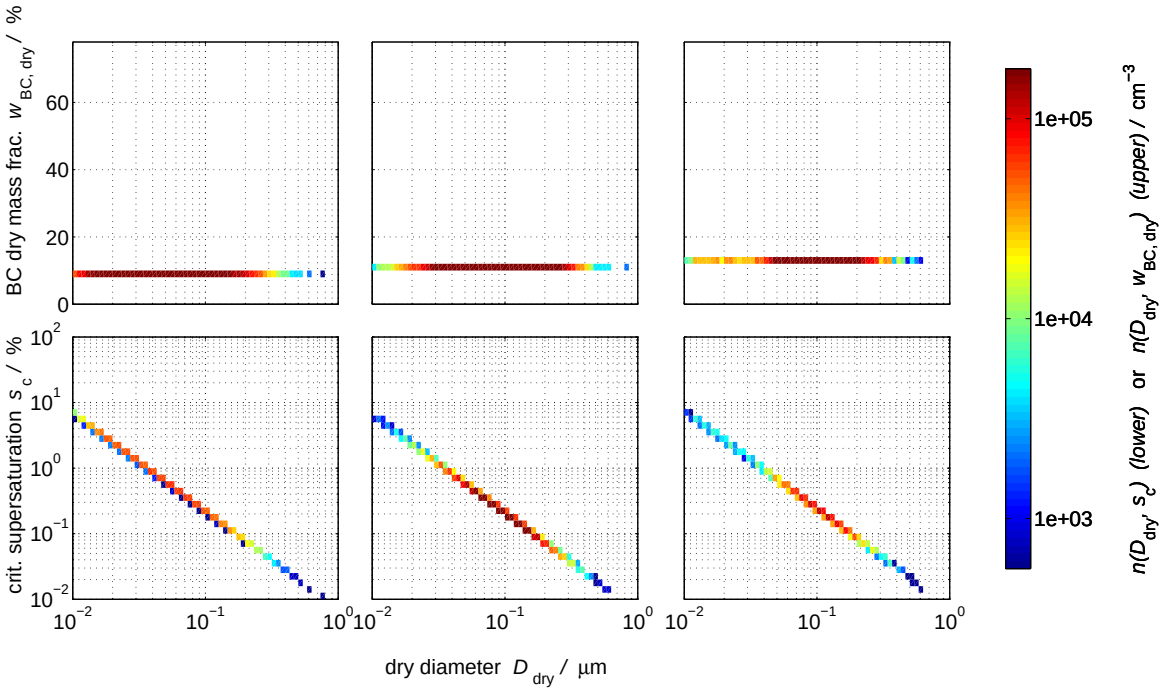

Figure 5.15: Composition averaged two-dimensional number concentration distribution $n(D_{\mathrm{dry}},\ w_{\mathrm{BC,dry}})$ at t_p = 1 h, 12 h, 24 h shown in the top panels and critical supersaturation, $n(D_{\mathrm{dry}}, s_c)$ shown in the bottom panels.

In this section, we investigate how the mixing state affects the cloud droplet fraction and amount of BC nucleation scavenging fraction. We compared the results from using fully-resolved particle populations to particle population where the composition has been averaged over the whole population. Case 2 serves as our reference case and is referred to as 'ref' and the composition-averaged case will be referred to as 'comp'. For this section, only the q_1 and q_4 profiles were used to show the two extremes in the amount of entrainment.

Consistent with *Ching et al.* (2012), we define the cloud droplet fraction, f_{N}, as the ratio of the cloud droplet number concentration, N_{d}, to the total number concentration of particles, N_{a}. We also define the nucleation-scavenged mass concentration of BC as the mass concentration of BC within the cloud droplets. The nucleation-scavenged mass fraction of

BC, f_{BC}, is the ratio of the BC mass concentration associated with the cloud droplets to the total BC mass concentration.

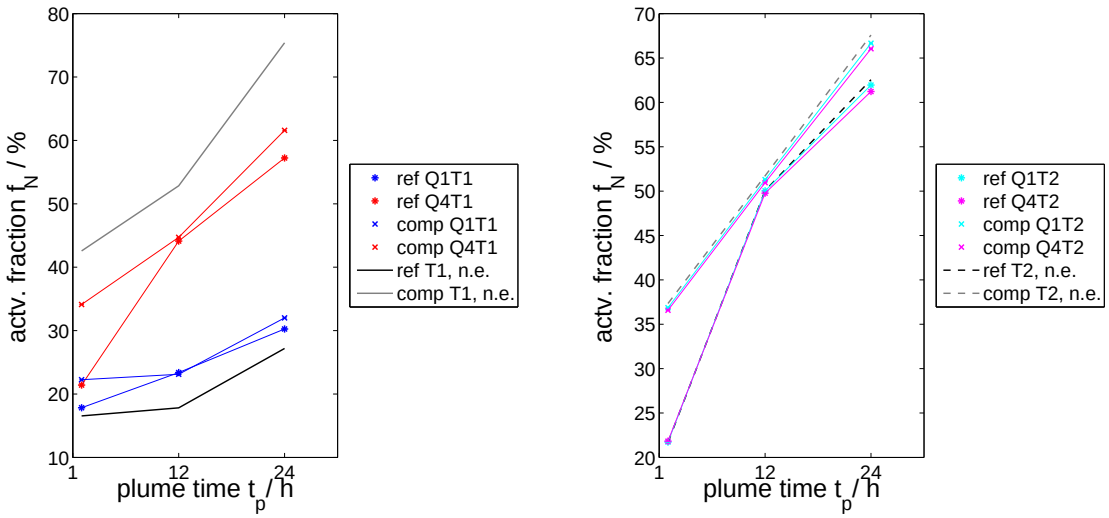

Figure 5.16: Cloud droplet fraction, f_{N}, for scenario T_1 (left) and T_2 (right).

The BC nucleation-scavenged mass fraction was affected by the amount of entainment, cooling rate, and the input particle population. Figure 5.16 shows the results for f_{n} for 'ref' and 'comp' plotted against the plume hour. The cloud droplet fraction, f_{N} increased 2%, 8% and 5% for t_{plume} =1, 12, and 24 h, respectively for scenario 'ref' q_1, T_1. In comparing entrainment amounts, f_{N} increased between 5%, 25% , and 30% for t_{plume} =1, 12 and 24 h, respectively for scenario 'ref' q_4, T_1. Alternatively, f_{N} decreased between 20 to 40% when the smallest amount of entrainment occurred and 10 to 20% when the largest amount of entrainment occurred. Along with the entrainment process, the cooling rate impacted the cloud droplet fraction as well. Seen in Figure 5.16, when using T_2 profiles, f_{N} only for $t_{\mathrm{plume}} = 24$ h between 0.5% and 1% for q_1 and q_4, respectively. The cloud droplet activation fraction increased with plume hour for both cooling rates. For example, 'ref' q_1, T_1 increased from 18% to 30%, while 'ref' q_4, T_1 scenario increased from 21% to 58% with plume time. Differences in the fraction resulted from the cooling rate, amount of entrainment, and length of time for which initial particle population aged. During t_{plume}=1 h, there was a large

amount of fresh particles, while the later hours contain aged particles. The aged particles were more hydrophilic and easier to activate, which is shown by the increase in f_{N}. When comparing 'ref' and 'comp' scenarios, 'comp' always overestimated f_{N} for plume hour 1 and 24, with the largest overestimation occuring for hour 1. For plume hour 12, the 'ref' and 'comp' scenarios are equal.

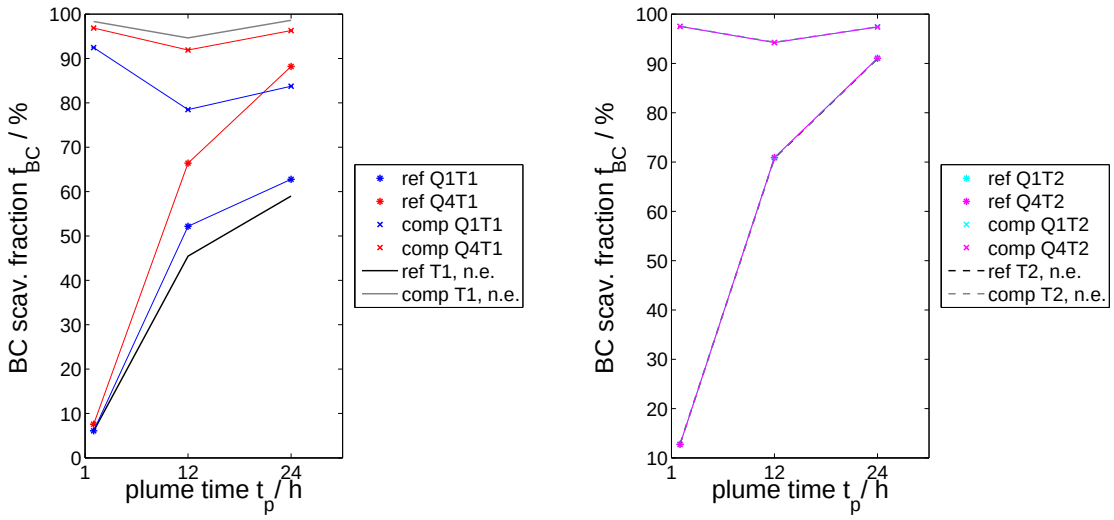

Figure 5.17: Nucleation-scavenged BC mass fraction, f_{BC}, for scenario T_1, T_2.

Figure 5.17 shows f_{BC} as a function of t_{plume}. Entrainment altered the f_{BC} the 'ref' and 'comp' when using T_1 profiles, but not T_2. The BC nucleation scavenging fraction, f_{BC} increased 5% for $t_{\mathrm{plume}} = 12$ and 24 h for scenario 'ref' q_1, T_1. The fraction increased 10% and 20% for $t_{\mathrm{plume}} = 12$ and 24 h for scenario 'ref' q_4, T_1. The same pattern was seen in f_{BC} where the profile increased with plume hour. The BC scavenging fraction showed a larger increase with plume hour than the activation fraction. For example, 'ref' Q_1, T_1 increased from 7% to 63%, while 'ref' Q_4, T_1 increase from 8% to 89% with increasing plume time. The comp scenarios were always higher than the 'ref' scenarios for f_{BC} with differences up to 85%. The percent difference decreased with plume hour. This is because the 'ref' scenario had the lowest w_{BC} during $t_{\mathrm{plume}} = 24$ h, which most closely matched the w_{BC} in the 'comp' scenario. The overestimation of f_{BC} in 'comp' was seen by *Ching et al.* (2012). These results

show that for these scenarios, it is more important to resolve the composition in order to accurately simulate the BC scavenging fraction and the activation fraction and entrainment alters f_{BC} depending the cooling rate.

Chapter 6

Conclusions

In this thesis, we tested the new model capability of PartMC-MOSAIC together with a cloud parcel model, which includes the process of entrainment of sub-saturated air into the cloud. With this model, we investigated how the black carbon mixing state impacts cloud microphysical properties when entrainment is included. First, we ran an idealized urban plume scenario, which tracked about 10,000 computational particles for 24 hours. Second, we took the particle populations at 1, 12 and 24 hours and input into a cloud parcel simulation for 1000 seconds. We prescribed temperature, pressure, and total specific humidity profiles during the parcel times. We presented three cases in this work. Case 1 used idealized temperature, pressure, and total specific humidity profiles to extend the study by *Ching et al.* (2012) to include entrainment. Case 2 used temperature and pressure data from a 3-D cloud resolving model to further investigate the impact of cooling rate and entrainment on cloud properties. Finally, Case 3 used composition-averaged particle populations initialize the cloud parcel and we use Case 2 as a reference case to compare the results.

For Case 1, the larger cooling rate, T_2 resulted in higher maximum supersaturation values, allowing for a higher cloud droplet number concentration (CDNC). The addition of entrainment in the cloud parcel model led to differences in the cloud microphysical properties. The smallest entrainment event, q_1, led to the smallest percent decrease in LWC and CDNC compared with the no entrainment case and the largest event, q_4, led to the largest decrease

in those quantities. At the end of the simulation, the CDNC differed by around 4% between q_1 and q_4. Additionally, the entrainment caused a broadening and shift towards smaller sizes for the number concentration size distribution.

Case 2, showed similar results to Case 1 when using T_2 profiles, while T_1 had a different pattern in the CDNC. For the T_1 scenarios, the relative humidity decreased more than the T_2 scenarios during the entrainment event, but increased to a very high supersaturation after the entrainment ended. This caused droplets to activate to a higher amount than the no entrainment scenario. The large variablity in the temperature profile with parcel time caused the differences seen in the CDNC. In the q_4, T_1, $t_{\text{plume}} = 12$ h scenario, the cloud was completely evaporated due to entrainment, in which a large amount hygroscopic background aerosols activated. The scenarios presented in this case showed showed similar broadening in the size distributions as seen in Case 1.

In Case 3, entrainment altered the cloud droplet fraction, f_{N}, and showed increases up to 30% for the 'ref' q_4, T_1 scenario and decreases of 1% for the 'ref' q_4, T_2 scenario. In the nucleation-scavenged mass fraction, f_{BC}, entrainment influenced T_1 scenarios with a 5% and 20% increase seen q_1 and q_4, respectively for $t_{\text{plume}} = 24$ h. The temporal patten in f_{N} and f_{BC} showed an increase with plume hour because the aged emissions were more likely to activate than fresh emissions. An overestimation for all plume hours was seen in the compostition averaged case compared to the reference case for f_{BC}. When comparing 'ref' and 'comp' cases for f_{N}, 'comp' always overestimated for plume hour 1 and 24, with the largest overestimation occuring for hour 1. For plume hour 12, the 'ref' and 'comp' cases were equal. These results show that for these scenarios, it is important to resolve the composition in order to accurately simulate the BC scavenging fraction and the activation fraction.

In the future, more cloud parcel simulations could be run using less idealized entrainment events. This would allow us to see how more variability in the input total specific humidity profiles influences the cloud microphysical quantities. Additionally, the cloud parcel could

be more realistic by including chemical processing. The effects of entrainment on the precipitation process would be another area of development by including collision-coalescence in the cloud parcel. Lastly, including semi-direct effects of black carbon in the parcel would allow us to investigate black carbon climate effects further.

Appendix A

Cloud parcel model equations

This appendix lists the equations that are implemented to form the cloud parcel code. The variables are explained in Appendix B.

$$P^0(T) = 611.2 \exp\left(7.45 \ln(10) \frac{T - 273.15}{T - 38}\right) \tag{A.1}$$

$$\frac{\partial P^0}{\partial T}(T) = P^0(T) 7.45 \ln(10) \frac{273.15 - 38}{(T - 38)^2} \tag{A.2}$$

$$\rho_{\text{air}} = M_{\text{air}} \frac{p}{RT} \tag{A.3}$$

$$U(T) = \frac{\Delta H_{\text{v}} \rho_{\text{w}}}{4T} \tag{A.4}$$

$$V(T) = \frac{4 M_{\text{w}} P^0(T)}{\rho_{\text{w}} RT} \tag{A.5}$$

$$\frac{\partial V}{\partial T}(T) = \left(\frac{1}{P^0(T)} \frac{\partial P^0}{\partial T}(T) - \frac{1}{T}\right) V(T) \tag{A.6}$$

$$W(T) = \frac{\Delta H_{\text{v}} M_{\text{w}}}{RT} \tag{A.7}$$

$$X(T) = \frac{4 M_{\text{w}} \sigma_{\text{w}}}{RT \rho_{\text{w}}} \tag{A.8}$$

$$Y(T) = \frac{2 k_{\text{a}}}{\alpha \rho_{\text{air}} c_{\text{p}}} \sqrt{\frac{2\pi M_{\text{air}}}{RT}} \tag{A.9}$$

$$Z(T) = \frac{2 D_{\text{v}}}{\alpha} \sqrt{\frac{2\pi M_{\text{w}}}{RT}} \tag{A.10}$$

$$V_{\text{comp}}(T) = \frac{T}{T_0} V_{\text{comp},0} \quad V_{\text{comp},0} \text{ is the computational volume at temperature } T_0 \tag{A.11}$$

$$\frac{\partial V_{\text{comp}}}{\partial T}(T) = \frac{V_{\text{comp},0}}{T_0} \tag{A.12}$$

$$= \frac{V_{\text{comp}}}{T} \tag{A.13}$$

$$k_{\text{a}} = 10^{-3}(4.39 + 0.071T) \tag{A.14}$$

$$k'_{\text{a}}(D_i) = \frac{k_{\text{a}}}{1 + Y/D_i} \tag{A.15}$$

$$\frac{\partial k'_{\text{a}}}{\partial D_i}(D_i) = \frac{k_{\text{a}} Y}{(D_i + Y)^2} \tag{A.16}$$

$$D_{\text{v}} = \frac{0.211 \cdot 10^{-4}}{p/p_0} \left(\frac{T}{273}\right)^{1.94} \tag{A.17}$$

$$D'_{\text{v}}(D_i) = \frac{D_{\text{v}}}{1 + Z/D_i} \tag{A.18}$$

$$\frac{\partial D'_{\text{v}}}{\partial D_i}(D_i) = \frac{D_{\text{v}} Z}{(D_i + Z)^2} \tag{A.19}$$

$$\kappa^a = \frac{M_{\text{w}} \rho_a}{M_a \rho_{\text{w}}} \qquad \text{assuming number of ions per dissociation is 1.} \tag{A.20}$$

$$\kappa_i = \sum_a \kappa^a \frac{V^a_{\text{dry}}}{V_{\text{dry}}} \tag{A.21}$$

$$a_{\text{w}i}(D_i) = \frac{D_i^3 - D_{i,\text{dry}}^3}{D_i^3 + (\kappa_i - 1) D_{i,\text{dry}}^3} \tag{A.22}$$

$$\frac{\partial a_{\text{w}i}}{\partial D_i}(D_i) = \frac{3 D_i^2 \kappa_i D_{i,\text{dry}}^3}{(D_i^3 + (\kappa_i - 1) D_{i,\text{dry}}^3)^2} \tag{A.23}$$

$$\begin{aligned} h_i(\delta, D_i, H) = k'_{\text{a}}(D_i)\delta - UV D'_{\text{v}}(D_i) \Bigg(H - \left(\frac{1}{1+\delta}\right) a_{\text{w}i}(D_i) \\ \times \exp\left(W \frac{\delta}{1+\delta} + \frac{X}{D_i} \frac{1}{1+\delta} \right) \Bigg) \end{aligned} \tag{A.24}$$

$$\begin{aligned} \frac{\partial h_i}{\partial \delta}(\delta, D_i, H) = k'_{\text{a}}(D_i) - \frac{UV D'_{\text{v}}(D_i) a_{\text{w}i}(D_i)}{(1+\delta)^2} \left(1 - W \frac{1}{1+\delta} + \frac{X}{D_i} \frac{1}{1+\delta} \right) \\ \times \exp\left(W \frac{\delta}{1+\delta} + \frac{X}{D_i} \frac{1}{1+\delta} \right) \end{aligned} \tag{A.25}$$

$$\frac{\partial h_i}{\partial D_i}(\delta, D_i, H) = \frac{\partial k'_{\mathrm{a}}}{\partial D_i}(D_i)\delta - UV\frac{\partial D'_{\mathrm{v}}}{\partial D_i}(D_i)H + UV\left(a_{\mathrm{w}i}(D_i)\frac{\partial D'_{\mathrm{v}}(D_i)}{\partial D_i} + D'_{\mathrm{v}}(D_i)\frac{\partial a_{\mathrm{w}i}}{\partial D_i}(D_i) - D'_{\mathrm{v}}(D_i)a_{\mathrm{w}i}(D_i)\frac{X}{D_i^2}\frac{1}{1+\delta}\right) \times \left(\frac{1}{1+\delta}\right)\exp\left(W\frac{\delta}{1+\delta} + \frac{X}{D_i}\frac{1}{1+\delta}\right) \tag{A.26}$$

$$\frac{\partial h_i}{\partial H}(\delta, D_i, H) = -UV\,D'_{\mathrm{v}}(D_i) \tag{A.27}$$

$$0 = h_i(\delta_i^*(D_i, H), D_i, H) \tag{A.28}$$

$$0 = \frac{d}{dD_i}h_i(\delta_i^*(D_i, H), D_i, H) = \frac{\partial h_i}{\partial \delta}(\delta_i^*(D_i, H), D_i, H)\frac{\partial \delta_i^*}{\partial D_i}(D_i, H) + \frac{\partial h_i}{\partial D_i}(\delta_i^*(D_i, H), D_i, H) \tag{A.29}$$

$$0 = \frac{d}{dH}h_i(\delta_i^*(D_i, H), D_i, H) = \frac{\partial h_i}{\partial \delta}(\delta_i^*(D_i, H), D_i, H)\frac{\partial \delta_i^*}{\partial H}(D_i, H) + \frac{\partial h_i}{\partial H}(\delta_i^*(D_i, H), D_i, H) \tag{A.30}$$

$$\frac{\partial \delta_i^*}{\partial D_i}(D_i, H) = -\frac{\frac{\partial h_i}{\partial D_i}(\delta_i^*(D_i, H), D_i, H)}{\frac{\partial h_i}{\partial \delta}(\delta_i^*(D_i, H), D_i, H)} \tag{A.31}$$

$$\frac{\partial \delta_i^*}{\partial H}(D_i, H) = -\frac{\frac{\partial h_i}{\partial H}(\delta_i^*(D_i, H), D_i, H)}{\frac{\partial h_i}{\partial \delta}(\delta_i^*(D_i, H), D_i, H)} \tag{A.32}$$

$$\dot{D}_i(D_i, H) = \frac{k'_{\mathrm{a}}(D_i)\delta_i^*(D_i, H)}{UD_i} \tag{A.33}$$

$$\frac{\partial \dot{D}_i}{\partial D_i}(D_i, H) = \frac{1}{UD_i}\frac{\partial k'_{\mathrm{a}}}{\partial D_i}(D_i)\delta_i^*(D_i, H) + \frac{1}{UD_i}k'_{\mathrm{a}}(D_i)\frac{\partial \delta_i^*}{\partial D_i}(D_i, H) - \frac{1}{UD_i^2}k'_{\mathrm{a}}(D_i)\delta_i^*(D_i, H) \tag{A.34}$$

$$\frac{\partial \dot{D}_i}{\partial H}(D_i, H) = \frac{k'_{\mathrm{a}}(D_i)}{UD_i}\frac{\partial \delta_i^*}{\partial H}(D_i, H) \tag{A.35}$$

$$\dot{H}_i(D_i, H) = -\frac{2\pi}{V(T)V_{\mathrm{comp}}(T)}D_i^2\dot{D}_i(D_i, H) \tag{A.36}$$

$$\frac{\partial \dot{H}_i}{\partial D_i}(D_i, H) = -\frac{2\pi}{V(T)V_{\mathrm{comp}}(T)}\left(2D_i\dot{D}_i(D_i, H) + D_i^2\frac{\partial \dot{D}_i}{\partial D_i}(D_i, H)\right) \tag{A.37}$$

$$\frac{\partial \dot{H}_i}{\partial H}(D_i, H) = -\frac{2\pi}{V(T)V_{\mathrm{comp}}(T)}D_i^2\frac{\partial \dot{D}_i}{\partial H}(D_i, H) \tag{A.38}$$

$$\dot{H}_{\text{env}}(D_1,\dots,D_N,H) = -\frac{1}{V(T)}\frac{\partial V}{\partial T}(T)\dot{T}H - \frac{1}{V_{\text{comp}}(T)}\frac{\partial V_{\text{comp}}}{\partial T}(T)\dot{T}H \tag{A.39}$$

$$\frac{\partial \dot{H}_{\text{env}}}{\partial D_i}(D_1,\dots,D_N,H) = 0 \tag{A.40}$$

$$\frac{\partial \dot{H}_{\text{env}}}{\partial H}(D_1,\dots,D_N,H) = -\frac{1}{V(T)}\frac{\partial V}{\partial T}(T)\dot{T} - \frac{1}{V_{\text{comp}}(T)}\frac{\partial V_{\text{comp}}}{\partial T}(T)\dot{T} \tag{A.41}$$

$$H = \frac{4m_{\text{w}}}{\rho_{\text{w}}V(T)V_{\text{comp}}(T)} \tag{A.42}$$

$$\dot{H}(D_1,\dots,D_N,H) = \sum_{i=1}^{N}\dot{H}_i(D_i,H) + \dot{H}_{\text{env}}(D_1,\dots,D_N,H) \tag{A.43}$$

$$\frac{\partial \dot{H}}{\partial D_i}(D_1,\dots,D_N,H) = \frac{\partial \dot{H}_i}{\partial D_i}(D_i,H) + \frac{\partial \dot{H}_{\text{env}}}{\partial D_i}(D_1,\dots,D_N,H) \tag{A.44}$$

$$\frac{\partial \dot{H}}{\partial H}(D_1,\dots,D_N,H) = \sum_{i=1}^{N}\frac{\partial \dot{H}_i}{\partial H}(D_i,H) + \frac{\partial \dot{H}_{\text{env}}}{\partial H}(D_1,\dots,D_N,H) \tag{A.45}$$

If $D_i < D_{i,\text{dry}}$ then we take

$$h_i(\delta,D_i,H) = k'_{\text{a}}(D_{i,\text{dry}})\delta - UVD'_{\text{v}}(D_{i,\text{dry}})H \tag{A.46}$$

$$\frac{\partial h_i}{\partial \delta}(\delta,D_i,H) = k'_{\text{a}}(D_{i,\text{dry}}) \tag{A.47}$$

$$\frac{\partial h_i}{\partial D_i}(\delta,D_i,H) = 0 \tag{A.48}$$

$$\frac{\partial h_i}{\partial H}(\delta,D_i,H) = -UVD'_{\text{v}}(D_{i,\text{dry}}) \tag{A.49}$$

$$\delta_i^*(D_i,H) = \frac{UVD'_{\text{v}}(D_{i,\text{dry}})H}{k'_{\text{a}}(D_{i,\text{dry}})} \tag{A.50}$$

$$\frac{\partial \delta_i^*}{\partial D_i}(D_i,H) = 0 \tag{A.51}$$

$$\frac{\partial \delta_i^*}{\partial H}(D_i,H) = \frac{UVD'_{\text{v}}(D_{i,\text{dry}})}{k'_{\text{a}}(D_{i,\text{dry}})} \tag{A.52}$$

$$\dot{D}_i(D_i,H) = \frac{k'_{\text{a}}(D_{i,\text{dry}})\delta_i^*(D_i,H)}{UD_{i,\text{dry}}} \tag{A.53}$$

$$\frac{\partial \dot{D}_i}{\partial D_i}(D_i,H) = 0 \tag{A.54}$$

$$\frac{\partial \dot{D}_i}{\partial H}(D_i,H) = \frac{k'_{\text{a}}(D_{i,\text{dry}})}{UD_{i,\text{dry}}}\frac{\partial \delta_i^*}{\partial H}(D_i,H) \tag{A.55}$$

$$\dot{H}_i(D_i,H) = -\frac{2\pi}{V(T)V_{\text{comp}}(T)}D_{i,\text{dry}}^2\dot{D}_i(D_i,H) \tag{A.56}$$

$$\frac{\partial \dot{H}_i}{\partial D_i}(D_i, H) = -\frac{2\pi}{V(T)V_{\text{comp}}(T)} D_{i,\text{dry}}^2 \frac{\partial \dot{D}_i}{\partial D_i}(D_i, H) \tag{A.57}$$

$$\frac{\partial \dot{H}_i}{\partial H}(D_i, H) = -\frac{2\pi}{V(T)V_{\text{comp}}(T)} D_{i,\text{dry}}^2 \frac{\partial \dot{D}_i}{\partial H}(D_i, H) \tag{A.58}$$

For equilibriation:

$$g_i(D_i, H) = h_i(0, D_i, H) \tag{A.59}$$

$$= H - a_{\text{w}i}(D_i) \exp\left(\frac{X}{D_i}\right) \tag{A.60}$$

$$\frac{\partial g_i}{\partial D_i}(D_i, H) = -\frac{\partial a_{\text{w}i}}{\partial D_i}(D_i) \exp\left(\frac{X}{D_i}\right) + a_{\text{w}i}(D_i) \exp\left(\frac{X}{D_i}\right) \frac{X}{D_i^2} \tag{A.61}$$

Appendix B

List of variables

This appendix provides the explanation of the variables used in Appendix A.

Symbol	Meaning	Numerical value
α	thermal accommodation coefficient	1.0
M_{air}	molecular weight of air	2.89644×10^{-2} kg mol^{-1}
M_{w}	molecular weight of water	18×10^{-3} kg mol^{-1}
M_i	molecular weight of aerosol species i	species dependent
c_{p}	specific heat capacity of air at constant pressure	1004 J kg^{-1}
ρ_{w}	density of water	1×10^3 kg m^{-3}
ρ_i	aerosol density	species dependent
κ_i	hygroscopicity of component i	species dependent
R	universal gas constant	8.314 J mol^{-1} K^{-1}
σ_{w}	surface tension (or surface energy) of water	0.073 J m^{-2}
ΔH_{v}	latent heat of vaporization of water	2.272×10^6 J kg^{-1}
p_0	standard surface pressure	101300 Pa
p	environmental air pressure	input (Pa)
T	environmental temperature	input (K)
D_{dry}	dry diameter of the aerosol particle	input (m)
V_{dry}	dry volume of the aerosol particle	input (m^3)
V^a_{dry}	dry volume of species a of the aerosol particle	input (m^3)

Symbol	Meaning	Numerical value
V_{comp}	computational volume	input (m^3)
D_{v}	diffusivity coefficient	function ($\mathrm{m}^2\,\mathrm{s}^{-1}$)
D'_{v}	corrected diffusivity coefficient	function ($\mathrm{m}^2\,\mathrm{s}^{-1}$)
δ^*	growth parameter	function
a_{w}	water activity	function
κ	overall hygroscopicity	function
ρ_{air}	air density	function
k_{a}	thermal conductivity of air	function ($\mathrm{J}\,\mathrm{m}^{-1}\,\mathrm{s}^{-1}\,\mathrm{K}^{-1}$)
k'_{a}	corrected thermal conductivity of air	function ($\mathrm{J}\,\mathrm{m}^{-1}\,\mathrm{s}^{-1}\,\mathrm{K}^{-1}$)
P^0	saturation vapor pressure	function (Pa)
D_i	droplet wet diameter	dynamical variable
m_{w}	mass of water vapor	
m_i	total mass of particle	
H	environmental relative humidity	dynamical variable
$\dot{H}_i$	relative humidity change due to particle i	
$\dot{H}_{\mathrm{env}}$	relative humidity change due to environment	

References

Ackerman, A. S., O. Toon, D. Stevens, A. Heymsfield, V. Ramanathan, and E. Welton (2000), Reduction of tropical cloudiness by soot, *Science*, *288*(5468), 1042–1047.

Albrecht, B. A. (1989), Aerosols, cloud microphysics, and fractional cloudiness, *Science*, *245*(4923), 1227–1230.

Baker, M., R. Corbin, and J. Latham (1980), The influence of entrainment on the evolution of cloud droplet spectra: I. a model of inhomogeneous mixing, *Quarterly Journal of the Royal Meteorological Society*, *106*(449), 581–598.

Barahona, D., and A. Nenes (2007), Parameterization of cloud droplet formation in large-scale models: Including effects of entrainment, *Journal of Geophysical Research: Atmospheres (1984–2012)*, *112*(D16).

Blyth, A. M., S. G. Lasher-Trapp, and W. A. Cooper (2005), A study of thermals in cumulus clouds, *Quarterly Journal of the Royal Meteorological Society*, *131*(607), 1171–1190.

Bond, T., et al. (2013), Bounding the role of black carbon in the climate system: A scientific assessment, *Journal of Geophysical Research: Atmospheres*.

Bond, T. C. (2007), Can warming particles enter global climate discussions?, *Environmental Research Letters*, *2*(4), 045,030.

Burnet, F., and J.-L. Brenguier (2007), Observational study of the entrainment-mixing process in warm convective clouds, *Journal of the atmospheric sciences*, *64*(6), 1995–2011.

Carpenter Jr, R. L., K. K. Droegemeier, and A. M. Blyth (1998), Entrainment and detrainment in numerically simulated cumulus congestus clouds. part i: General results, *Journal of the atmospheric sciences*, *55*(23), 3417–3432.

Ching, J., N. Riemer, and M. West (2012), Impacts of black carbon mixing state on black carbon nucleation scavenging: Insights from a particle-resolved model, *Journal of Geophysical Research: Atmospheres (1984–2012)*, *117*(D23).

Chỳlek, P., G. Videen, D. Ngo, R. G. Pinnick, and J. D. Klett (1995), Effect of black carbon on the optical properties and climate forcing of sulfate aerosols, *Journal of Geophysical Research*, *100*(D8), 16,325–16.

Cooper, W. A., S. G. Lasher-Trapp, and A. M. Blyth (2013), The influence of entrainment and mixing on the initial formation of rain in a warm cumulus cloud, *Journal of the Atmospheric Sciences*, *70*(6), 1727–1743.

Fan, J., R. Zhang, W.-K. Tao, and K. I. Mohr (2008), Effects of aerosol optical properties on deep convective clouds and radiative forcing, *Journal of Geophysical Research: Atmospheres (1984–2012)*, *113*(D8).

Gardiner, K., N. W. Trethowan, J. M. Harrington, C. E. Rossiter, and I. A. Calvert (1993), Respiratory health effects of carbon black: a survey of european carbon black workers., *British journal of industrial medicine*, *50*(12), 1082–1096.

Gelbard, F., and J. H. Seinfeld (1980), Simulation of multicomponent aerosol dynamics, *Journal of colloid and Interface Science*, *78*(2), 485–501.

Goldberg, E. D. (1985), Black carbon in the environment: properties and distribution.

Hansen, J., M. Sato, A. Lacis, and R. Ruedy (1997), The missing climate forcing, *Philosophical Transactions of the Royal Society of London. Series B: Biological Sciences*, *352*(1350), 231–240.

IPCC (2013), Climate change 2013: Synthesis report. contribution of working groups i, ii and iii to the fifth assessment report of the intergovernmental panel on climate change, *Tech. rep.*, IPCC, Geneva, Switzerland, core Writing Team, Pachauri, R.K and Reisinger, A. (eds.).

Jeong, C.-H., P. K. Hopke, E. Kim, and D.-W. Lee (2004), The comparison between thermal-optical transmittance elemental carbon and aethalometer black carbon measured at multiple monitoring sites, *Atmospheric Environment*, *38*(31), 5193–5204.

Johari, H. (1992), Mixing in thermals with and without buoyancy reversal, *Journal of the atmospheric sciences*, *49*(16), 1412–1426.

Koch, D., and A. D. Genio (2010), Black carbon semi-direct effects on cloud cover: review and synthesis, *Atmospheric Chemistry and Physics*, *10*(16), 7685–7696.

Koren, I., Y. J. Kaufman, L. A. Remer, and J. V. Martins (2004), Measurement of the effect of amazon smoke on inhibition of cloud formation, *Science*, *303*(5662), 1342–1345.

Lasher-Trapp, S. G., W. A. Cooper, and A. M. Blyth (2005), Broadening of droplet size distributions from entrainment and mixing in a cumulus cloud, *Quarterly Journal of the Royal Meteorological Society*, *131*(605), 195–220.

Latham, J., and R. Reed (1977), Laboratory studies of the effects of mixing on the evolution of cloud droplet spectra, *Quarterly Journal of the Royal Meteorological Society*, *103*(436), 297–306.

Lesins, G., P. Chylek, and U. Lohmann (2002), A study of internal and external mixing scenarios and its effect on aerosol optical properties and direct radiative forcing, *Journal of Geophysical Research: Atmospheres (1984–2012)*, *107*(D10), AAC–5.

McFarquhar, G. M., and H. Wang (2006), Effects of aerosols on trade wind cumuli over the indian ocean: Model simulations, *Quarterly Journal of the Royal Meteorological Society*, *132*(616), 821–843.

Myhre, G., C. Myhre, B. Samset, and T. Storelvmo (2013), Aerosols and their relation to global climate and climate sensitivity, *Nature Education Knowledge*, *4*(5), 7.

Ogren, J., and R. Charlson (1983), Elemental carbon in the atmosphere: Cycle and lifetime, *Tellus B*, *35*(4), 241–254.

Penner, J., H. Eddleman, and T. Novakov (1993), Towards the development of a global inventory for black carbon emissions, *Atmospheric Environment. Part A. General Topics*, *27*(8), 1277–1295.

Petters, M., and S. Kreidenweis (2007), A single parameter representation of hygroscopic growth and cloud condensation nucleus activity, *Atmospheric Chemistry and Physics*, *7*(8), 1961–1971.

Petters, M. D., A. J. Prenni, S. M. Kreidenweis, P. J. DeMott, A. Matsunaga, Y. B. Lim, and P. J. Ziemann (2006), Chemical aging and the hydrophobic-to-hydrophilic conversion of carbonaceous aerosol, *Geophysical research letters*, *33*(24).

Petzold, A., et al. (2013), Recommendations for reporting" black carbon" measurements, *Atmospheric Chemistry and Physics*, *13*(16), 8365–8379.

Prenni, A. J., M. D. Petters, S. M. Kreidenweis, P. J. DeMott, and P. J. Ziemann (2007), Cloud droplet activation of secondary organic aerosol, *Journal of Geophysical Research: Atmospheres (1984–2012)*, *112*(D10).

Riemer, N., and M. West (2013), Quantifying aerosol mixing state with entropy and diversity measures, *Atmospheric Chemistry and Physics*, *13*(22), 11,423–11,439.

Riemer, N., M. West, R. A. Zaveri, and R. C. Easter (2009), Simulating the evolution of soot mixing state with a particle-resolved aerosol model, *Journal of Geophysical Research: Atmospheres (1984–2012)*, *114*(D9).

Riemer, N., M. West, R. Zaveri, and R. Easter (2010), Estimating black carbon aging time-scales with a particle-resolved aerosol model, *Journal of Aerosol Science*, *41*(1), 143–158.

Schell, B., I. J. Ackermann, H. Hass, F. S. Binkowski, and A. Ebel (2001), Modeling the formation of secondary organic aerosol within a comprehensive air quality model system, *Journal of Geophysical Research. D. Atmospheres*, *106*, 28.

Scorer, R. (1957), Experiments on convection of isolated masses of buoyant fluid, *Journal of Fluid Mechanics*, *2*(06), 583–594.

Scorer, R., and F. Ludlam (1953), Bubble theory of penetrative convection, *Quarterly Journal of the Royal Meteorological Society*, *79*(339), 94–103.

Seinfeld, J. H., and S. N. Pandis (2012), *Atmospheric chemistry and physics: from air pollution to climate change*, John Wiley & Sons.

Spracklen, D., K. Pringle, K. Carslaw, M. Chipperfield, and G. Mann (2005), A global offline model of size-resolved aerosol microphysics: I. model development and prediction of aerosol properties, *Atmospheric Chemistry and Physics Discussions*, *5*(1), 179–215.

Squires, P. (1958), Penetrative downdraughts in cumuli, *Tellus*, *10*(3), 381–389.

Stier, P., J. H. Seinfeld, S. Kinne, J. Feichter, and O. Boucher (2006), Impact of nonabsorbing anthropogenic aerosols on clear-sky atmospheric absorption, *Journal of Geophysical Research: Atmospheres (1984–2012)*, *111*(D18).

Stommel, H. (1947), Entrainment of air into a cumulus cloud: (paper presented 27 december 1946 at the annual meeting, ams, cambridge, massachusetts), *Journal of Meteorology*, *4*(3), 91–94.

Telford, J. W. (1975), Turbulence, entrainment, and mixing in cloud dynamics, *pure and applied geophysics*, *113*(1), 1067–1084.

Telford, J. W., and S. K. Chai (1980), A new aspect of condensation theory, *pure and applied geophysics*, *118*(2), 720–742.

Twomey, S. (1977), The influence of pollution on the shortwave albedo of clouds, *Journal of the atmospheric sciences*, *34*(7), 1149–1152.

Videen, G., D. Ngo, and P. Chýlek (1994), Effective-medium predictions of absorption by graphitic carbon in water droplets, *Opt. Lett.*, *19*(21), 1675–1677, doi: 10.1364/OL.19.001675.

Weingartner, E., H. Burtscher, and U. Baltensperger (1997), Hygroscopic properties of carbon and diesel soot particles, *Atmospheric Environment*, *31*(15), 2311–2327.

Whitby, E. R., and P. H. McMurry (1997), Modal aerosol dynamics modeling, *Aerosol science and technology*, *27*(6), 673–688.

Zaveri, R. A., and L. K. Peters (1999), A new lumped structure photochemical mechanism for large-scale applications, *Journal of Geophysical Research: Atmospheres (1984–2012)*, *104*(D23), 30,387–30,415.

Zaveri, R. A., R. C. Easter, and L. K. Peters (2005a), A computationally efficient multicomponent equilibrium solver for aerosols (mesa), *Journal of Geophysical Research: Atmospheres (1984–2012)*, *110*(D24).

Zaveri, R. A., R. C. Easter, and A. S. Wexler (2005b), A new method for multicomponent activity coefficients of electrolytes in aqueous atmospheric aerosols, *Journal of Geophysical Research: Atmospheres (1984–2012)*, *110*(D2).

Zaveri, R. A., R. C. Easter, J. D. Fast, and L. K. Peters (2008), Model for simulating aerosol interactions and chemistry (mosaic), *Journal of Geophysical Research: Atmospheres (1984–2012)*, *113*(D13).

Zaveri, R. A., J. C. Barnard, R. C. Easter, N. Riemer, and M. West (2010), Particle-resolved simulation of aerosol size, composition, mixing state, and the associated optical and cloud condensation nuclei activation properties in an evolving urban plume, *Journal of Geophysical Research: Atmospheres (1984–2012)*, *115*(D17).